

Project no.:

608608

Project acronym:

MiReCOL

Project title:

Mitigation and remediation of leakage from geological storage

Collaborative Project

Start date of project: 2014-03-01

Duration: 3 years

D5.2

The effects of stress on leakage through faults and fracture networks

Revision: 1

Organisation name of lead contractor for this deliverable:

TNO

Project co-funded by the European Commission within the Seventh Framework Programme		
Dissemination Level		
PU	Public	X
PP	Restricted to other programme participants (including the Commission Services)	
RE	Restricted to a group specified by the consortium (including the Commission Services)	
CO	Confidential , only for members of the consortium (including the Commission Services)	

Deliverable number:	D5.2
Deliverable name:	The effects of stress on leakage through faults and fracture networks
Work package:	WP 5: Remediation linked to transport properties of faults and fracture networks
Lead contractor:	TNO

Status of deliverable		
Action	By	Date
Submitted (Author(s))	A. Lavrov	26.09.2016.
	A. Antropov	20.09.2016.
	D. Karas	20.09.2016.
	B. Orlic	04.11.2016.
Verified (WP-leader)	B. Orlic	07.11.2016.
Approved (SP-leader)	H. Cremer	10.11.2016

Author(s)		
Name	Organisation	E-mail
A. Lavrov	SINTEF	Alexandre.Lavrov@sintef.no
A. Antropov	NIS	Antropov.AV@nis.eu
D. Karas	NIS	dusan.karas@nis.eu
B. Orlic	TNO	bogdan.orlic@tno.nl

Public abstract
<p>The MiReCOL project investigates existing and new techniques for remediation and mitigation of leakage from geological CO₂ storage. Assessment of potential leakage through faults and fractured caprocks is of primary concern for geological CO₂ storage sites. Faults and fracture networks can act either as permeability barriers or preferential pathways for fluid flow, depending on the infill and the stresses acting on them. Hence, faults and fractures can be open and conductive at some time and closed and non-conductive at other times.</p> <p>This study investigates the effect of <i>in-situ</i> stress alterations on flow through faults and fractures in the cap rock. Study results are largely published as: (i) an Energy Procedia paper presented at the 13th International Conference on Greenhouse Gas Control Technologies (GHGT-13) held in Lausanne (Lavrov <i>et al.</i>, 2016, <i>Diversion of CO₂ to nearby reservoir compartments for remediation of unwanted CO₂ migration. GHGT-13, Lausanne</i>) and (ii) a peer-reviewed paper in the Journal of Petroleum Exploration and Production Technology (Lavrov, A., 2016, <i>Fracture permeability under normal stress: a fully computational approach. DOI 10.1007/s13202-016-0254-6</i>).</p> <p>First paper describes a semi-analytical model of flow through a vertical fracture penetrating cap rock taking into account the stress-dependent fracture permeability. The semi-analytical model of leakage developed in this study allows a quick estimation of the leakage potential without the need for a complicated and time-consuming coupled reservoir simulation. The model enables to obtain first-order estimates of the leakage rate. Second paper describes a numerical approach for predicting the fracture permeability as a function of the effective normal stress taking into</p>

account the fracture roughness. The computational approach provides an insight into the actual mechanics of the fracture deformation under stress, and the effect of stress on the permeability. The third (unpublished) part of this report describes a workflow for coupled stress-flow reservoir simulations implemented in the numerical geomechanical simulator Visage. The workflow is applied on a semi-synthetic model of the Becej natural CO₂ field to investigate the effect of stress on CO₂ flow through a hypothetical fault in the overburden. For the simulated cases and selected ranges of input parameters, the effects of injection-induced stress changes on flow rates through faults were minor.

TABLE OF CONTENTS

SUMMARY	2
1 EFFECT OF <i>IN-SITU</i> STRESS ALTERATIONS ON FLOW THROUGH FAULTS AND FRACTURES IN THE CAP ROCK	3
1.1 Introduction	3
1.2 Semi-analytical model of leakage through a vertical fracture	5
1.3 Effect of <i>in-situ</i> stresses on leakage flow rate	8
1.4 Discussion and conclusion	10
Acknowledgements	11
References	11
2 FRACTURE PERMEABILITY UNDER NORMAL STRESS	13
Acknowledgment.....	13
2.1 Introduction	14
2.2 Computational workflow	16
2.3 Results	19
2.3.1 Brittle rock	19
2.3.2 Ductile rock	21
2.4 Discussion.....	23
2.5 Conclusions	25
References	25
Tables	28
Figures	29
3 COUPLED NUMERICAL MODELLING OF STRESS-DEPENDENT CO ₂ FLOW THROUGH FAULTS IN THE CAP ROCK	43
3.1 Introduction	43
3.2 Simulation cases	43
3.3 Model setup	44
3.3.1 Model geometry and flow properties.....	44
3.3.2 Geomechanical grid	45
3.3.3 Geomechanical properties	46
3.3.4 Permeability update	47
3.3.5 Geomechanical model initialization	49
3.3.6 Flow model initialization	49
3.4 Simulation results	49
3.4.1 Cases without gas injection	49
3.4.2 Cases with gas injection.....	52
3.5 Conclusions	54
References	54

SUMMARY

The MiReCOL project investigates existing and new techniques for remediation and mitigation of leakage from geological CO₂ storage sites. WP5 of this project is concerned with remediation options linked to transport properties of faults and fracture networks. This report is the second deliverable of WP5 (D5.2). The report investigates the effect of *in-situ* stress alterations on flow through faults and fractures in the cap rock. Deliverable D5.2 consists of three parts:

- 1) an Energy Procedia paper presented at the 13th International Conference on Greenhouse Gas Control Technologies (GHGT-13) held in Lausanne:
Lavrov et al., 2016, Diversion of CO₂ to nearby reservoir compartments for remediation of unwanted CO₂ migration. GHGT-13, Lausanne;
- 2) a peer-reviewed paper published in the *Journal of Petroleum Exploration and Production Technology*:
Lavrov, A., 2016, Fracture permeability under normal stress: a fully computational approach. DOI 10.1007/s13202-016-0254-6;
- 3) a report on coupled numerical simulations of stress-dependent CO₂ flow through faults in the cap rock, conducted on the semi-synthetic model of the Becej natural CO₂ field, Serbia.

First paper (by SINTEF, NIS and TNO) describes a semi-analytical model of flow through a vertical fracture penetrating cap rock taking into account the stress-dependent fracture permeability. The semi-analytical model of leakage developed in this study allows a quick estimation of the leakage potential without the need for a complicated and time-consuming coupled reservoir simulation. The model enables to obtain first-order estimates of the leakage rate.

Second paper (by SINTEF) presents a numerical approach for predicting the fracture permeability as a function of the effective normal stress taking into account the fracture roughness. This computational approach provides an insight into the actual mechanics of the fracture deformation under stress, and the effect of stress on the permeability.

The third and final part of this report (by NIS) describes a workflow for coupled stress-flow reservoir simulations implemented in the numerical geomechanical simulator Visage. The workflow is applied on a semi-synthetic model of the Becej natural CO₂ field to investigate the effect of stress on CO₂ flow through a hypothetical fault in the overburden. For the simulated cases and selected ranges of input parameters, the effects of injection-induced stress changes on flow rates through faults were minor.

1 EFFECT OF *IN-SITU* STRESS ALTERATIONS ON FLOW THROUGH FAULTS AND FRACTURES IN THE CAP ROCK

13th International Conference on Greenhouse Gas Control Technologies, GHGT-13, 14-18 November 2016, Lausanne, Switzerland

Effect of *in-situ* stress alterations on flow through faults and fractures in the cap rock

Andrey Antropov, Alexandre Lavrov, Bogdan Orlic

Abstract

Cap-rock integrity is of paramount importance during injection and subsequent long-term storage of CO₂ in the subsurface. Pre-existing (natural) and man-induced fractures in the cap rock represent potential flow paths out of the storage formation. In this study, a first-order semi-analytical model of flow through a vertical fracture penetrating cap rock is constructed taking the stress-dependent fracture permeability into account. The model is then applied to study the effects of *in-situ* stress normal to fracture on the flow rate through the fracture. The flow rate increases nonlinearly with the reservoir pressure, which is due to a combined effect of nonlinear fracture deformation law and the cubic law governing the flow rate.

1.1 Introduction

Cap-rock integrity is of paramount importance during injection of CO₂ and during subsequent long-term storage of CO₂ in the subsurface. Fractures and faults in the cap rock represent potential flow paths for CO₂ migration out of the storage formation. Pre-existing sealing fractures and faults may open and thereby become hydraulically conductive if the compressive normal stress acting on the fracture plane is reduced during injection or during subsequent lifetime of the storage site.

Stress changes leading to fracture opening can be caused by natural geological processes, but may also result from the stress re-distribution accompanying the injection of CO₂ into the reservoir [1, 2]. For instance, injection into a reservoir is known to increase the total horizontal stresses in the reservoir and to reduce the total (and effective) horizontal stresses in the overburden (Fig. 1) [3]. Such stress alteration will lead to dilation, and possibly the opening of pre-existing, natural vertical fractures that often exist in siliciclastic (shales, claystone) and evaporitic (anhydrite) cap rocks. Fracture reopening will increase the permeability of the overlying formation, which may allow CO₂ to migrate upwards through the cap rock. For example, at the In Salah CO₂ injection project in Algeria, CO₂ injection in well KB-502 caused tensile opening of an existing fracture zone in the caprock and upward migration of the injected CO₂ into the lower part of the caprock [4, 5]. Another type of fractures that may create flow paths through the cap rock are fractures in the near-well area. Since a wellbore serves as a stress concentrator, alterations of *in-situ* stresses caused by injection are likely to be amplified in the vicinity of the well. Such amplified stresses may induce new fractures or activate the already existing ones, enabling upward migration of CO₂ across the cap rock.

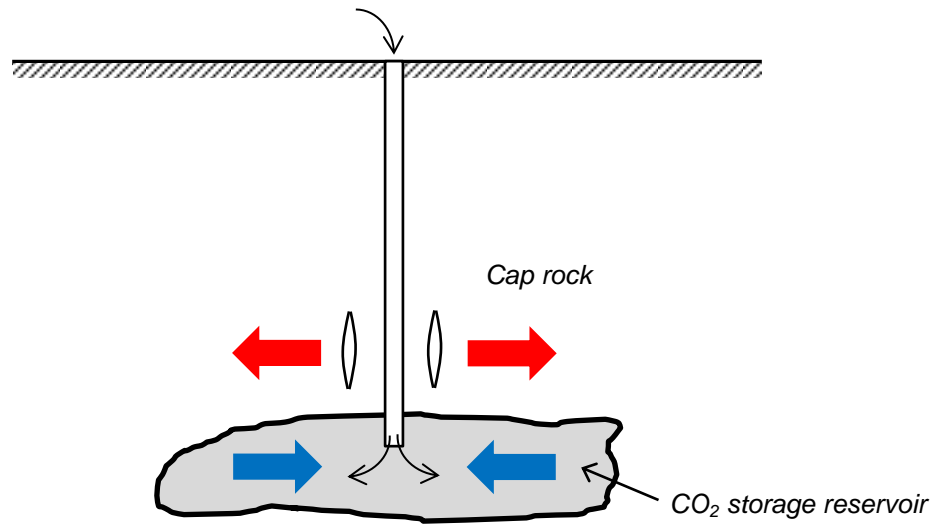


Fig. 1. (a) Schematic view of vertical fracture opening in the cap rock caused by CO₂ injection into the underlying reservoir. Blue arrows indicate increase of horizontal total stresses in the reservoir (stresses becoming more compressive). Red arrows indicate decrease of horizontal total stresses in the overburden (stresses becoming less compressive). Aperture of pre-existing, natural vertical fractures in the overburden is likely to increase as a result of these stress changes. This will increase the permeability of the cap rock.

In this study, we focus on the effect of a single, individual vertical fracture in the cap rock on leakage from a CO₂ storage reservoir. The effect of an individual vertical fracture on CO₂ leakage was previously addressed in refs. [6, 7]. However, geomechanical effects were neglected in those earlier studies, and only the hydraulic problem was treated. In reality, the permeability of a fracture (and thus the flow through the fracture) depends on the effective normal stress acting on the fracture plane and given by:

$$\sigma'_n = \sigma_n - p \quad (1)$$

where σ'_n is the effective normal stress; σ_n is the total normal stress; p is the fluid pressure inside the fracture. It is assumed in Eq. (1) that the Biot effective stress coefficient for the fracture deformation is equal to one, which is a common assumption for fractures in geomechanics. When the effective normal stress increases, either due to an increase in the *in-situ* horizontal stress or due to a reduction in the fluid pressure, the fracture closes, and its permeability decreases. Conversely, when the effective normal stress decreases, e.g. due to a fluid pressure increase caused by fluid injection or due to a reduction in the *in-situ* horizontal stresses, the fracture opens, and its permeability increases. The decrease in the permeability in the former case and the increase in the latter are typically nonlinear: it takes more effort to close the fracture as its aperture becomes smaller since more asperities come into contact, and the normal stiffness of the fracture increases.

In this paper, remediation by flow diversion is first analyzed using a synthetic test case and then applied to a real field case. The findings inferred from these cases are discussed. Finally, more general conclusions are drawn on the use of flow diversion as a remediation measure in the context of geological CO₂ storage.

Consider a vertical fracture (a "joint") penetrating the cap rock from the reservoir to an upper aquifer. In reality, it can be an isolated fracture, a fracture network or a pre-existing fault. For the sake of simplicity, the case of an isolated fracture is considered in this study. During CO₂ injection, the fluid pressure front might eventually reach the fracture, and the fluid pressure in the fracture will increase. This will induce the flow (of CO₂ or brine) in the fracture in the vertical direction unless the fracture is completely closed and thus has zero permeability (this may happen e.g. if the fracture is filled with gouge or is mineralized). At the same time, the fracture might start opening as the pressure increases along the fracture height. This will increase the fracture permeability. Therefore, we are dealing here with a two-way coupled problem: The fracture aperture affects the fluid flow, and the fluid pressure affects the fracture aperture. The coupling strength depends on the fracture properties, in particular the normal stiffness.

As the CO₂ injection proceeds, the horizontal *in-situ* stresses in the cap rock may eventually decrease. This will further increase the fracture permeability and thus the leakage rate.

Fractures may have different orientation. Even in the same fracture set, the fracture orientations may slightly vary. Thus, the normal stress acting on each vertical fracture is different unless the horizontal *in-situ* stresses are isotropic. Moreover, different normal stresses may act on different parts of the same fracture if the fracture surface is not a perfect plane. These considerations suggest that the total normal stress plays a crucial role in determining the fracture permeability.

The objective of this study was to investigate the effect of a single vertical fracture in the cap rock on the integrity of a CO₂ storage site. To this end, we construct a simple semi-analytical model in Section 2 that can be used to estimate the leakage flow rate as a function of the reservoir pressure. The model is then applied to demonstrate the effect of *in-situ* stresses on the leakage flow rate in Section 3. The paper concludes with a discussion and recommendations on CO₂ storage site selection and pressure management that would take into account geomechanical effects and stress-dependent fracture permeability.

1.2 Semi-analytical model of leakage through a vertical fracture

The geometry of the model is shown in Fig. 2. The fracture height and length are equal to H and L , respectively. The fracture width is equal to w and can be different at different vertical locations. However, the fracture width is assumed to be the same at all points located at the same depth, i.e. at a given z .

There are many correlations between the normal stress and the fracture permeability available in the literature. For instance, the following correlation was reported for shale in ref. [8]:

$$k = k_0 \exp(-C'\sigma'_n) \quad (2)$$

where C' is a fitting parameter, equal to e.g. 0.27 for Kimmeridge shale [8]; k_0 is the permeability of a fracture at zero effective normal stress. Two examples of k vs. σ_n dependency are shown in Fig. 3, for two different values of C' .

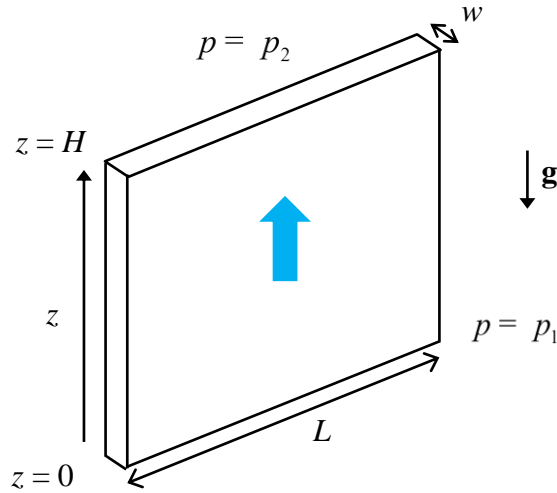


Fig. 2. Geometry of the vertical fracture in the cap rock. Blue arrow indicates the direction of flow (upwards). Fracture width, height, and horizontal length are denoted by w , H , and L , respectively.

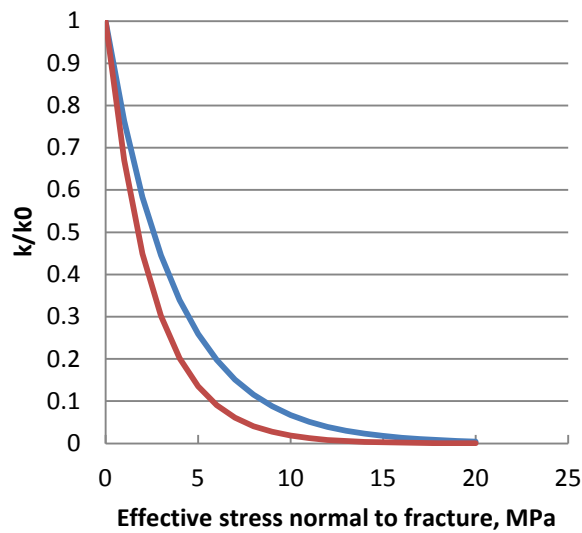


Fig. 3. Fracture permeability vs. effective normal stress for $C' = 0.27$ (blue) and $C' = 0.4$ (red), according to Eq. (2).

Assuming single-phase flow (e.g. CO₂ dissolved in brine), the superficial fluid velocity in the fracture along the vertical direction is given by:

$$v = -\frac{w^2}{12\mu} \frac{d}{dz} (p + \rho_f gz) \quad (3)$$

where ρ_f and μ are the density and the dynamic viscosity of the fluid, respectively; g is the acceleration of gravity; z is the vertical coordinate (Fig. 2). The aperture, w , in Eq. (1) should be hydraulic rather than mechanical aperture. In this model, we make no distinction between the two, thereby implying that the mechanical and hydraulic apertures are equal. Since the fracture is assumed to have the same aperture at all locations at a given z , the horizontal components of the superficial fluid velocity are equal to zero at all locations inside the fracture.

We assume that the fracture permeability can be approximated *locally* with Eq. (2). For a Newtonian fluid, the local fracture permeability is given by $w^2/12$. Thus, the aperture is given by:

$$w = w_0 \exp(-C'\sigma'_n / 2) \quad (4)$$

where w_0 is the aperture at zero effective normal stress. Assume that the horizontal *in-situ* stress acting normal to the fracture plane is a linear function of depth:

$$\sigma_n = \sigma_0 - \beta\rho_b g z \quad (5)$$

where σ_0 is the horizontal *in-situ* stress at the bottom of the fracture ($z = 0$); ρ_b is the bulk density of the rock; β is a dimensionless coefficient. In extensional tectonic regime, e.g. in stable intercontinental areas, $\beta < 1$. In compressional stress environment, e.g. in tectonically active areas, $\beta > 1$. Substituting Eqs. (4) and (5) into Eq. (3) yields the following pressure equation for the fracture:

$$\frac{dp}{dz} + \rho_f g = -\frac{12\mu Q}{Lw_0^3} \exp[C(\sigma_0 - \beta\rho_b g z - p)] \quad (6)$$

where Q is the flow rate through the fracture (m³/s), and $C = 3C'/2$.

After introducing dimensionless pressure, flow rate, z -coordinate, σ_0 , rock bulk weight, and fluid bulk weight as follows:

$$\begin{aligned} \tilde{p} &= \frac{p}{\rho_f g H} , \\ \tilde{Q} &= \frac{12\mu Q}{L\rho_f g w_0^3} , \\ \tilde{z} &= z/H , \\ \tilde{\sigma}_0 &= C\sigma_0 , \\ \tilde{\gamma}_b &= C\beta\rho_b g H , \\ \tilde{\gamma}_f &= C\rho_f g H , \end{aligned} \quad (7)$$

the pressure equation reduces to:

$$\frac{d\tilde{p}}{d\tilde{z}} + \tilde{Q} \exp(\tilde{\sigma}_0 - \tilde{\gamma}_b \tilde{z} - \tilde{\gamma}_f \tilde{p}) + 1 = 0 \quad (8)$$

As a boundary condition, we specify pressure, P_2 at the top of the fracture (Fig. 2):

$$\tilde{p} = \tilde{p}_2 \quad \text{at} \quad \tilde{z} = 1 \quad (9)$$

1.3 Effect of *in-situ* stresses on leakage flow rate

We now perform computations for different flow rates, Q , and different *in-situ* stress values at the fracture bottom, σ_0 . The dimensional input parameters for the simulations are listed in Table 1. Dimensionless parameters derived from Table 1 using Eqs. (7) are listed in Table 2. Table 2 demonstrates how the number of parameters has been reduced by non-dimensionalization.

Eq. (8) with the boundary condition given by Eq. (9) was solved numerically using the spatial discretization step $\Delta\tilde{z} = 10^{-4}$. Computations were performed for a wide range of flow rates and for two values of the *in-situ* stress at the fracture bottom (see Tables 1 and 2).

The results in form of pressure curves at different flow rates are presented in Figure 4 for two values of the dimensionless horizontal *in-situ* stress: $\tilde{\sigma}_0 = 10.8$ (Figure 4a) and $\tilde{\sigma}_0 = 8.1$ (Figure 4b). The red lines in Figure 4 represent the fracture reopening pressure. Fracture reopening occurs when the fluid pressure in the fracture is equal to the total normal stress, $p = \sigma_n$. In dimensionless parameters, the fracture reopening is thus given by:

$$\tilde{p} = \frac{\tilde{\sigma}_0 - \tilde{\gamma}_b \tilde{z}}{\tilde{\gamma}_f} \quad (10)$$

As evident from Figure 4, the pressure stays below the fracture reopening pressure at all flow rates except the highest one.

Flow rate through the fracture increases nonlinearly with the fluid pressure applied at the fracture bottom. This nonlinearity is a combined result of two mechanisms: the nonlinear fracture deformation law (Eq. (4)) and the "cubic law" describing the dependency of the flow rate on the local fracture aperture (Eq. (3)). According to Eq. (4), the fracture aperture increases faster as the effective stress becomes smaller, i.e. as the pressure increases and the fracture opens up. According to the "cubic law" [9, 10], the flow rate is proportional to w^3 [cf. Eq. (3)]. Thus, both mechanisms result in the flow rate increasing more rapidly as the pressure in the reservoir builds up.

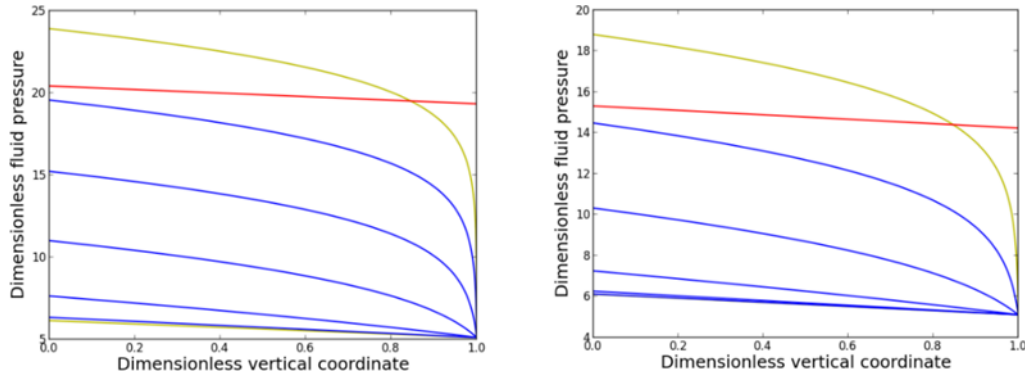


Fig. 4. Dimensionless fluid pressure in the fracture as a function of depth at different leakage rates. The red line shows the fracture reopening pressure. The top yellow line corresponds to $\tilde{Q}=12.2$. The bottom yellow curve corresponds to $\tilde{Q}=1.22 \cdot 10^{-5}$. The blue curves correspond, in ascending order, to $\tilde{Q}=1.22 \cdot 10^{-4}$, $1.22 \cdot 10^{-3}$, $1.22 \cdot 10^{-2}$, $1.22 \cdot 10^{-1}$, 1.22 . The dimensionless horizontal *in-situ* total stress, $\tilde{\sigma}_0$, is equal to 10.8 (a) or 8.1 (b). The bottom yellow line is indistinguishable from the bottom blue line in (b).

Table 1. Dimensional input parameters for semi-analytical simulations.

Dimensional parameter	Value
C, Pa^{-1}	$0.27 \cdot 10^{-6}$
β	0.4
$\rho_b, \text{kg/m}^3$	2700
$\rho_f, \text{kg/m}^3$	1000
$g, \text{m/s}^2$	9.8
H, m	200
L, m	100
$\mu, \text{Pa}\cdot\text{s}$	0.001
W_0, m	0.001
p_2, Pa	$10 \cdot 10^6$
σ_0, Pa	$40 \cdot 10^6; 30 \cdot 10^6$
$Q, \text{m}^3/\text{s}$	$10^{-6} \dots 1$

Table 2. Dimensionless input parameters for semi-analytical simulations; based on Table 1 and Eqs. (7).

Dimensionless parameter	Value
$\tilde{\gamma}_b = C\beta\rho_b gH$	0.572
$\tilde{\gamma}_f = C\rho_f gH$	0.529
$\tilde{p}_2 = p_2 / (\rho_f gH)$	5.102
$\tilde{Q} = 12\mu Q / (L\rho_f gW_0^3)$	$1.22 \cdot 10^{-5} \dots 12.2$
$\tilde{\sigma}_0 = C\sigma_0$	10.8; 8.1

1.4 Discussion and conclusion

The semi-analytical model constructed in Section 2 is a simple and fast computational tool that enables risk assessment of leakage through a vertical fracture in the cap rock caused by pressure increase in the reservoir. Computations presented in Section 3 demonstrate that the nonlinear fracture deformation may lead to a rapid increase of the fracture permeability and thus the leakage rate when the fluid pressure front propagates upwards in the fracture. It is therefore important to characterize fractures present or suspected in the cap rock. *In-situ* investigation of fracture properties at CO₂ storage sites is, in practice, difficult or impossible. Numerical simulations of fracture deformation and flow under stress can therefore be used, as explicated in another recent publication from the MiReCOL project, ref. [11].

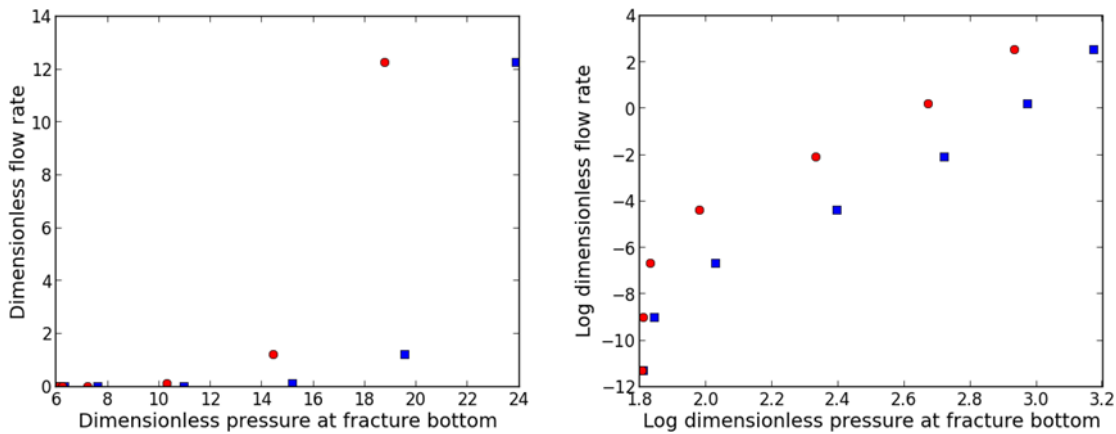


Fig. 5. Dimensionless flow rate through the fracture as a function of fluid pressure at the bottom of the fracture (the "reservoir pressure") for $\tilde{\sigma}_0 = 10.8$ (blue squares) and $\tilde{\sigma}_0 = 8.1$ (red circles) in linear-linear (a) and log-log (b) coordinates.

The in-situ stress normal to fracture is of paramount importance for leakage prediction through vertical fractures, as Fig. 5 shows. Therefore, in-situ stress measurements are crucial for risk assessment of leakage in CO₂ storage sites. Such measurements can be performed by means of extended leakoff tests, breakout analysis, deformation rate analysis, etc. Fractures can have different orientations in the cap rock. The fractures normal to the minimum horizontal stress have the lowest reopening pressure and thus are most prone to leakage, other parameters being equal.

The variation of the fracture reopening pressure with the fracture orientation led recently one of the authors to introduce two new concepts in drilling-related geomechanics: the *spectrum* of fracture reopening pressures and the *spectrum* of lost-circulation pressures [12, 13]. These are to replace the commonly used (e.g., in drilling) *fracture reopening pressure* and *lost-circulation pressure*. The analyses presented in this paper demonstrate that the knowledge of the fracture reopening pressure *spectrum* is essential for leakage risk assessment in CO₂ storage projects, too.

Nonlinearity of the leakage rate as a function of the reservoir pressure evident in Figure 5 suggests that the role of monitoring becomes even more important as the injection proceeds. Increasing the reservoir pressure by 1 bar at a later stage of injection is likely to have a larger impact on the leakage risk than the same increase at the beginning of injection.

The semi-analytical model of leakage through a vertical fracture in the cap rock developed in this study allows a quick estimation of the leakage potential without the need for a complicated and time-consuming coupled reservoir simulation. The model enables to obtain first-order estimates of the leakage rate. Based on this initial assessment, more detailed, site-specific numerical models (e.g. coupled reservoir-geomechanical models) can be developed.

Such detailed coupled simulations are indeed required for assessment of long-term effects of CO₂ injection on the stress field and, thus, on the fracture permeability. Such effects are due to the *stress path*, i.e. the change of the total *in-situ* stresses in the reservoir and in the cap rock caused by the pore pressure variation in the reservoir [14]. During CO₂ injection, the total horizontal stresses in the reservoir increase, while the total horizontal stresses in the cap rock slightly decrease. This will increase the permeability of the vertical fractures penetrating the cap rock, as evident from Fig. 5 (compare the red and blue data points).

The importance of fracture characterization in the cap rock of a CO₂ storage site is obvious from our analysis. Fracture properties are crucial for application of even the simplest models, such as the semi-analytical model introduced in Section 2. In particular, not only fracture permeabilities, but also fracture aperture, orientation, morphology, and stress-displacement behaviour should be characterized by field and laboratory measurements as accurately as possible. This will improve the overall risk assessment of CO₂ storage sites in both short-term and long-term perspectives.

Acknowledgements

Research reported in this paper has been conducted with funding from the European Commission FP7 project MIRECOL (www.mirecol-co2.eu), Grant Agreement No. 608608. The project received additional funding from Statoil, ENGIE and Shell.

References

- [1] Lavrov A Dynamics of stresses and fractures in reservoir and cap rock under production and injection. *Energy Procedia* 2016; 86: 381-90.
- [2] Orlic B, Heege Jt, Wassing B Assessing the integrity of fault- and top seals at co2 storage sites. *Energy Procedia* 2011; 4: 4798-805.
- [3] Fjær E, Holt RM, Horsrud P, Raaen AM, Risnes R. *Petroleum related rock mechanics*. 2nd ed. Amsterdam: Elsevier; 2008.
- [4] Shi J-Q, Sinayuc C, Durucan S, Korre A Assessment of carbon dioxide plume behaviour within the storage reservoir and the lower caprock around the kb-502 injection well at in salah. *International Journal of Greenhouse Gas Control* 2012; 7: 115-26.
- [5] Rinaldi AP, Rutqvist J Modeling of deep fracture zone opening and transient ground surface uplift at kb-502 co2 injection well, in salah, algeria. *International Journal of Greenhouse Gas Control* 2013; 12: 155-67.
- [6] Selvadurai APS Fluid leakage through fractures in an impervious caprock embedded between two geologic aquifers. *Advances in Water Resources* 2012; 41: 76-83.

- [7] Zeidouni M Analytical model of leakage through fault to overlying formations. *Water Resources Research* 2012; 48: n/a-n/a.
- [8] Gutierrez M, Øino LE, Nygård R Stress-dependent permeability of a de-mineralised fracture in shale. *Marine and Petroleum Geology* 2000; 17: 895-907.
- [9] Brown SR Fluid flow through rock joints: The effect of surface roughness. *J. Geophys. Res. B* 1987; 92: 1337-47.
- [10] Zimmerman RW, Kumar S, Bodvarsson GS Lubrication theory analysis of the permeability of rough-walled fractures. *International Journal of Rock Mechanics and Mining Sciences & Geomechanics Abstracts* 1991; 28: 325-31.
- [11] Lavrov A Fracture permeability under normal stress: A fully computational approach. *Journal of Petroleum Exploration and Production Technology* 2016; 1-14.
- [12] Lavrov A. *Lost circulation: Mechanisms and solutions*. Oxford: Elsevier; 2016.
- [13] Lavrov A From fracture gradient to the spectrum of lost-circulation pressures: A paradigm shift? *Energy procedia, proceedings of ghgt-13 (this volume)*. 2016.
- [14] Holt RM, Gheibi S, Lavrov A. Where does the stress path lead? Irreversibility and hysteresis in reservoir geomechanics. Arma paper 16-496 presented at the 50th us rock mechanics / geomechanics symposium, houston, texas, USA, 26-29 june 2016. In.; 2016.

2 FRACTURE PERMEABILITY UNDER NORMAL STRESS

Fracture permeability under normal stress: a fully computational approach

Alexandre Lavrov

SINTEF Petroleum Research, Trondheim, Norway

Email: alexandre.lavrov@sintef.no

Tel.: +47 98 28 66 58

Abstract: Fractures contribute significantly to the overall permeability of naturally- or hydraulically-fractured reservoirs. In the cap rock, fractures may provide unwanted pathways for reservoir or stimulation fluids. Predicting fluid flow in naturally-fractured rocks under production or fluid injection requires that permeability of a single, rough-walled fracture be well understood and accurately described as a function of the effective stress. The lack of information about the properties of fractures at depth calls for a numerical approach that would enable predicting the fracture permeability as a function of the effective normal stress. Such fully computational approach is developed in this study. The fracture deformation is calculated by solving the contact problem using the finite-element method. At each deformation step, the steady-state fluid flow in the fracture is computed in two orthogonal directions using the lubrication theory approximation, in order to evaluate the permeability and the hydraulic aperture of the fracture. The computational approach is tested on two examples: a "brittle rock" (linear elastic) and a "ductile rock" (linear elastic perfectly plastic). Both mechanical and hydraulic behaviour of the fracture under cyclic normal loading are found to be in qualitative agreement with the results obtained in a number of published experimental studies. The computational approach provides an insight into the actual mechanics of the fracture deformation under stress, and the effect of the latter on the permeability. In particular, hysteresis in the fracture roughness is obtained with the "ductile rock" suggesting that (at least some) fractured rocks may retain "memory" about their loading history imprinted in the fracture landscapes.

Acknowledgment

The research leading to these results received funding from the European Union Seventh Framework Programme (FP7/2007-2013), subprogramme ENERGY.2013.5.2.1 "Mitigation and remediation of leakage from geological storage", under grant agreement No. 608608 ("Mitigation and remediation of CO₂ leakage"). The project receives additional funding from Statoil, GDF SUEZ and Shell.

2.1 Introduction

The importance of fracture for fluid flow in subsurface rocks has been recognised in hydrology, geophysics and reservoir engineering for at least three decades. In petroleum engineering, the naturally-fractured reservoirs (carbonates, gas shale) stand out as a subject of their own, because of their remarkably different behaviour (Aguilera 1980). Naturally-fractured reservoirs are those where fractures contribute crucially to storage and / or permeability. In reality, *all* rocks contain fractures, spanning in size from microcracks at grain scale to master joints extending for hundreds of meters (Twiss and Moores 2007).

Fracture permeability is a function of (i) the average opening of the fracture (which is often called the mechanical aperture); (ii) the roughness of the fracture faces caused by asperities. The roughness creates tortuous flow paths for the fluids (Brown 1987; Muralidharan et al. 2004). Hydraulic aperture of a fracture, w_h , is defined as the aperture of a smooth-walled conduit that has the same permeability as the real rough-walled fracture (Brown 1987; Zimmerman et al. 1991). The permeability of a fracture is thereby equal to $w_h^2/12$.

Note that the terms "mechanical aperture", "average aperture" and "mean aperture" are used interchangeably throughout this manuscript, just as they are in modern rock mechanical and hydrogeological literature.

When compressive normal stresses in the rock are increased, a fracture closes, and its permeability declines. At the same time, the fracture stiffness increases since more contacts between the fracture faces are created, and the area of the existing contacts increases (Chen et al. 2000; Pyrak-Nolte and Morris 2000). Similar effects, i.e. fracture closure and permeability reduction, are observed when the fluid pressure inside the fracture is reduced. Apart from direct reduction of the aperture, fracture closing increases the flow tortuosity since more asperities come into contact, and the flowing fluid has to go around them. This effectively increases the length of streamlines and pathlines, further reducing the hydraulic aperture of the fracture.

Unloading of a fracture, i.e. reduction of the normal stress, is usually accompanied with hysteresis in the fracture permeability: the fracture permeability is different during unloading from what it was at the same stress during loading (Gutierrez et al. 2000). Hysteresis of the fracture permeability under normal loading is a manifestation of a more general irreversibility of rock deformation that also includes, e.g., the "stress memory" capacity of rocks (Becker et al. 2010; Lavrov 2005).

Depletion of oil and gas reservoirs is known to be accompanied with fracture closure, which is one of the reasons for notoriously low recovery factors in naturally-fractured reservoirs (e.g. recovery factors down to 10-15% in some fractured carbonates). A recent study suggests that stress-dependent fracture permeability can reduce the cumulative ten-year production from an unconventional gas field by 10% (Aybar et al. 2014). Designing hydrocarbon production from and fluid injection into such fields requires a good grasp of the basic mechanisms affecting fracture behaviour during depletion and injection. It also calls for quantitative estimates of fracture permeability as a function of drawdown (reservoir pressure reduction).

It should be noted that very little information about fracture morphology (incl. roughness) and properties of the fracture network is available in practice when a field is developed. This information is usually gathered by interpreting image logs (acoustic or electric). Such logs show only traces of the fractures on the borehole wall. The resolution of the currently available equipment is not sufficient to quantify the fracture aperture, let alone provide information about fracture roughness. Under these circumstances, use of analogues, e.g. fractured outcrop rocks, for deriving fracture behaviour of fractures at depth becomes difficult, if possible at all, since fracture properties at depth can only be guessed.

The inaccessibility of fractures at depth, and unavailability of information on their properties, motivate the development of a computational approach that would allow an engineer to derive fracture properties such as stiffness and permeability from the limited information about the rock and fractures that is available. The first objective of this study is to demonstrate the viability of such approach for a fracture subject to normal stress.

Many empirical and semi-empirical fracture deformation laws have been proposed in the literature over the past 40 years. These laws are typically obtained for specific rocks. Each of such laws is therefore not particularly useful for other rocks. A number of empirical and semi-empirical laws governing fracture deformation under normal stress are discussed in (Gangi 1978; Malama and Kulatilake 2003). As pointed out in (Gangi 1978), the empirical and semi-empirical laws, albeit useful for matching the experimental data for a specific rock, provide no insight into the physical mechanisms of stress-dependent fracture permeability.

The limited validity and applicability of empirical and semi-empirical fracture deformation laws has motivated the development of numerical models of fracture deformation under normal stress. Most of these models are based on the approach of a "bed of nails" advocated in (Gangi 1978). In that study, asperities were considered as a collection of cylinders deforming independently of each other. It was shown that "nails" of different shapes could be used and could bring about the same fracture deformation law as the cylinders, provided that the length distribution of the "nails" is adjusted accordingly. A similar approach was taken in (Brown and Scholz 1986) where the Hertzian model was used to describe the interaction between asperities in contact. Independent interaction of asperities in models of this kind is a crude approximation. Another drawback of these models is the need for their calibration in terms of micromechanical parameters that cannot be easily obtained from a direct rock mechanical test. Despite the above weaknesses, tuning the model parameters enabled a good approximation of the measured normal stress vs fracture closure curves in (Brown and Scholz 1986; Gangi 1978). The Hertzian model was used to describe contact interaction between asperities also in a number of subsequent studies, e.g. (Lespinasse and Sausse 2000). A simplified description of the contact interaction was employed also in the work of (Pyrak-Nolte and Morris 2000) and (Detwiler and Morris 2014) who modelled asperities as circular cylinders behaving elastically at any stress.

It should be noted that, even though the above mentioned simplified treatments of fracture deformation do provide a valuable insight into the mechanics of fracture closure, it is difficult to establish a relationship between the parameters of such models and measurable rock properties. Modern finite-element codes offer a more accurate, and

consistent, description of contact interactions, without the major simplifications used in the above earlier works. In addition, the hard contact model implemented e.g. in the finite-element package ABAQUS and used in this study, involves only measurable, macro-scale properties of the rock, such as the Young's modulus and the Poisson's ratio, and is therefore more suitable for practical applications. Unlike its empirical and semi-empirical counterparts, the finite-element model of the contact problem allows one to study directly the effect of different factors, such as the rock plasticity, on the fracture deformation.

It should be noted that most of the experiments on fracture deformation and fracture permeability under stress have been performed on brittle, crystalline rocks such as granite, quartzite, marble etc. Studies on rocks showing some degree of plasticity, e.g. shale, are rare. Experiments of (Gutierrez et al. 2000) performed on Kimmeridge shale revealed irreversible, hysteretic fracture deformation under cyclic normal load. The fracture had nonmatching rough walls in that study. As a result, it was not possible to completely close such fracture by applying normal load. Even at normal stresses on the order of or higher than the unconfined compressive strength of the shale, the fracture permeability was several orders of magnitude higher than the matrix permeability of the rock. In contrast, experiments performed on an artificial, smooth-walled fracture using another shale (Opalinus Clay) demonstrated that the permeability of such fracture could be reduced virtually down to matrix permeability by applying a sufficiently large normal stress (Cuss et al. 2011). The above two studies demonstrate the essential role of asperities in governing the mechanical and hydraulic behaviour of fractures in a ductile rock. It should be noted that asperities also have a significant impact on particle transport. In particular, surface roughness gives rise to hydrodynamic dispersion during particle transport in fractures (Bauget and Fourar 2008; Cumbie and McKay 1999; Koyama et al. 2008; Nowamooz et al. 2013).

The role of plastic deformation in contact interactions between asperities was recognised and confirmed *via* SEM analyses already by (Brown and Scholz 1986). However, their plasticity model, being part of the Hertzian contact model, was severely oversimplified.

The objectives of this study, in addition to demonstrating the viability of the computational approach, were: to look into the effect of rock ductility (plasticity) on fracture permeability under normal stress; to look into the effect that normal stress might have on the roughness-induced anisotropy of the fracture permeability, in a relatively brittle rock and in a relatively ductile rock.

2.2 Computational workflow

The numerical workflow used for deriving fracture permeability as a function of normal stress in this work is as follows:

- 1) Generate two fracture surfaces. This is done numerically in this study. Alternatively, profilometry can be performed on geological samples of a fractured rock.
- 2) Use the two landscapes obtained in 1) to make two rock blocks (prisms), with each of the two landscapes being a face on one of the prisms. The prisms are then placed so that the two rough sides face each other (Figure 1).

- 3) Import the two rock blocks into a finite-element software.
- 4) Fix one block and apply a desired history of normal loading-unloading to the other block, under displacement control.
- 5) At each displacement step, export the distribution of the fracture aperture and construct an updated fracture aperture landscape.
- 6) For each exported distribution of aperture, perform fracture flow simulations to derive the fracture permeability (the hydraulic aperture).

Items 1, 2 and 3 in the above list are pre-processing. Item 5 is post-processing. Items 4 and 6 are the actual numerical simulations.

The recursive subdivision technique was used in this study to generate two fracture faces numerically (step 1 in the above list) (Fournier et al. 1982). Both fracture surfaces were generated using the same parameters, in particular the Hurst exponent (a parameter linked to the fractal dimension of the fracture surfaces) equal to 0.7, and had the same in-plane dimensions of 32 cm × 32 cm. The Hurst exponent is typically around 0.8 for natural fractures in rocks (Detwiler and Morris 2014). The in-plane grid spacing was equal to 1 cm, thus the fracture plane had 33 nodes in the *x*- and *y*-directions. The discretization was thus quite coarse. However, as shown by (Schmittbuhl et al. 2008), viscous flow in a fracture is controlled by long wavelengths of the fracture aperture landscape, at least when the fracture is opened. Therefore, as a first approximation, a coarse model was deemed sufficient. Using a fine grid would induce a prohibitive computational cost for the FEM model of mechanical deformation since the mechanical model was 3D, while the flow model was effectively 2D. All numerical computations in the workflow were performed on a desktop computer in this study. The relatively coarse resolution is sufficient to demonstrate the viability of our fully-computational approach. Finer grids can be used in future work.

It should be noted that the procedure described above and used for generating the fracture faces numerically in this study implies that fracture faces do not match at the beginning of the simulation. According to (Gangi 1978), this is a reasonable conjecture since, even in the case where the fracture faces could potentially be matching (e.g. freshly formed tensile fracture without shear displacement in hydraulic fracturing), the fracture will most likely be kept opened at some spots by gouge (small broken pieces of rock dislodged from the fracture faces). The latter would play the role of asperities even in the rare cases where the fracture faces could match.

The grid spacing of 1 cm ensured that the lubrication theory approximation would hold in flow simulations (step 6 in the above list). It should be noted that, instead of numerical generation of the fracture landscape, a real landscape could be obtained from a real rock sample using e.g. mechanical profilometry (Lespinasse and Sausse 2000) or laser profilometry (Młynarczyk 2010; Schmittbuhl et al. 2008).

A structured mesh of hexahedral elements was then generated in both blocks (step 2 in the above list). The two meshed blocks are shown in Figure 1. The two blocks were then imported into a finite-element code (item 3 in the above list). ABAQUS was used in this study, but any other FEM code capable of handling contact problems could be used as well.

ABAQUS is a commercially-available general-purpose finite-element code widely used for solving problems in solid mechanics. In this work, static stress analysis of fracture deformation under normal displacement was performed with ABAQUS. The following boundary conditions were applied on the bottom block: rollers at the bottom side ($z = 0$), the front side ($y = 0$) and the left-hand side ($x = 0$). See Figure 1 for the coordinate system. For the top block, z -displacement was applied at the top side. The loading was thus displacement-controlled. The intention was to reproduce the boundary conditions of a laboratory test used to study fracture deformation and flow.

After the finite-element simulation of fracture deformation was completed, the reaction force on the top surface of the top block was extracted. From this force, the averaged applied stress was calculated at each displacement step. Furthermore, the distribution of the contact opening was exported for each displacement step. This data was then used to construct an updated fracture aperture profile (step 5 in the above list).

For each updated fracture profile, a steady-state flow simulation was performed to assess the fracture permeability and the hydraulic aperture. To this end, the updated fracture profiles were imported into a fracture flow code, and a steady-state simulation of unidirectional flow of an incompressible Newtonian fluid was performed by applying a pressure gradient in the x -direction, i.e. between the sides $x = 0$ and $x = 32$ cm of the fracture. It should be noted that the fracture permeability is usually so much greater than the matrix permeability that matrix porosity and permeability were neglected in this study, and only flow inside the fracture was considered (with no matrix-fracture fluid exchange and no poroelastic effects in the matrix).

The fracture flow code solved the problem under the assumptions of the lubrication theory approximation. These assumptions are as follows (Zimmerman et al. 1991):

- (i) the inertial effects are negligible, i.e. the Reynolds number is smaller than 1;
- (ii) the velocity gradient in the fracture plane is much smaller than in the direction normal to fracture. This means in practice that the standard deviation of the aperture distribution is smaller than the largest wave length of the aperture profile.

Under the above assumptions, the flow equation is given by (Brown 1987; Keller et al. 1999):

$$\frac{\partial}{\partial x} \left(\frac{w^3}{12} \frac{\partial p}{\partial x} \right) + \frac{\partial}{\partial y} \left(\frac{w^3}{12} \frac{\partial p}{\partial y} \right) = 0 \quad (1)$$

where p is the fluid pressure inside the fracture; w is the local fracture aperture; x , y are Cartesian coordinates in the fracture plane. Eq. (1) was solved on a regular Cartesian grid using the finite-volume method described and benchmarked elsewhere (Lavrov 2014). It should be noted that numerical modelling of this type has been used for evaluation of fracture permeability in many previous studies, e.g. (Brown 1987; Koyama et al. 2008).

From the flow simulation (step 6 in the above list), the hydraulic fracture aperture was obtained as a function of the normal stress or displacement. Other outputs, at each loading step, included: distributions of fluid pressure and velocity in the fracture plane; maximum and average (mechanical) aperture of the fracture.

The numerical roadmap laid out above was tested on two examples:

- A) a linear-elastic rock ("brittle rock");
- B) an elastic perfectly plastic rock ("ductile rock").

The "brittle rock" may serve as a model for a fracture in a brittle, hard, crystalline rock. The "ductile rock" may serve as a model for a fracture in a soft, sedimentary rock showing significant plasticity, such as some shales.

2.3 Results

2.3.1 Brittle rock

The material properties of the rock are given in Table 1. The rock was linear elastic and might serve as analogue to a hard rock under stresses that do not exceed its yield point.

The two blocks were initially placed in such way that the initial mechanical aperture (the average distance between the rough fracture faces) was equal to 2 mm. There were no contact spots between the fracture faces at the beginning of the simulation. The displacement of the top surface of the top block was then increased from 0 to 5 mm so as to close the fracture. Since the material was linear elastic, the deformation was reversible, and no loading-unloading cycles were therefore performed in this simulation.

The averaged stress at the top surface of the top block *vs* applied displacement is shown in Figure 2 (solid line, diamond markers). The solid line in Figure 2 is quite nonlinear even though the rock is linear elastic. The nonlinearity was due to the fracture progressively closing as the displacement increased. The number and area of the contact spots were increasing with displacement, making the fracture effectively stiffer. This behaviour is well-known from laboratory tests, e.g. (Pyrak-Nolte and Morris 2000). The rate of stiffness increase depends on the rate of formation of new contacts as the fracture surfaces are pressed against each other.

The plot in Figure 2 is qualitatively similar to the stress-displacement plots in (Koyama et al. 2008; Malama and Kulatilake 2003). The displacement values represented by the solid line in Figure 2 contains both, the deformation (closure) of the fracture and the deformation (compression) of the bulk rock. As mentioned in (Koyama et al. 2008), the rightmost part of the solid curve corresponds to the elastic deformation of the bulk rock and is therefore linear in this simulation. The linear component of the deformation is plotted as a dashed line with triangular markers in Figure 2. We now follow the procedure described in (Koyama et al. 2008) to extract the fracture deformation curve from these simulation data. Shifting the solid line leftwards so that it now passes through the origin produces the dashed line with square markers in Figure 2. Shifting the dashed straight line with triangular markers leftwards, so that it now passes through the origin, produces the other dashed line with square markers in Figure 2. Subtracting one dashed line with square markers from the other produces the dotted line, which is the *fracture deformation* curve. Its shape is similar to the fracture deformation curve in (Koyama et al. 2008). All deformation of the bulk rock material has been removed from the displacement represented by the dotted curve. The dotted curve represents the pure fracture deformation.

The fracture deformation curve in Figure 2 has a vertical asymptote at 1.4 mm which, according to (Koyama et al. 2008), signifies the mechanical aperture of the fracture (i.e.

the mean aperture) at zero normal stress. It is the theoretical maximum of the relative normal displacement of the fracture faces that can be achieved by increasing the compressive stress on the fracture.

Analysis of the fracture aperture distributions at subsequent displacement steps has shown that the fracture faces first touched each other when the applied displacement became equal to 1.0 mm. The greatest value of the local fracture aperture as a function of the applied displacement is shown in Figure 3 (dashed line). It is evident from Figure 3 that the fracture became completely closed *mechanically* at the last loading step, i.e. at the applied displacement of 5 mm. The flow through the fracture in the x -direction ceased, however, already at the displacement of 2 mm, as the hydraulic aperture data suggest (solid curve in Figure 3). Figure 4 illustrates the decay of the mechanical aperture (average distance between the fracture faces) as the stress increases. The shape of the curve in Figure 4 resembles the respective plot obtained in a laboratory experiment on a granitic rock (Chen et al. 2000). The main qualitative difference between the curve in (Chen et al. 2000) and the curve in Figure 4 is that zero aperture was not reached in the former. In the simulation, a zero aperture is eventually reached as the stress becomes sufficiently high. In a real test, the bulk rock may break or the loading capacity of the equipment may be exceeded before that happens.

Note that the hydraulic aperture shown in Figure 3 was obtained when the pressure gradient was applied in the x -direction in the flow simulations, i.e. in the horizontal direction in Figure 5. In the right-hand part of the fracture, a region of small aperture existed from the very beginning (blue region in Figure 5a). As the loading proceeded, this region was closing first, until it completely blocked the flow in the x -direction (Figure 5b). The flow was blocked because the fracture became completely closed along its right-hand side ($x = 0.32$ m), while a substantial percentage of the fracture area was still mechanically opened, i.e. had nonzero local aperture.

It should be noted that, if the fracture were larger, the fluid would probably be able to find a way around and to bypass the closed area. However, since all fractures, in practice, are finite, the percolating flow path would sooner or later cease to exist at some displacement value, and the hydraulic aperture would drop to zero. In the case of a real, rough-walled fracture with poorly matching faces and/or with gouge deposited inside the fracture, the fracture is likely to remain mechanically opened at some spots when the flow stops. The exact displacement at which the flow stops is expected to depend on the initial aperture, the fracture roughness distribution, and the in-plane dimensions of the fracture.

The difference between the concepts of the hydraulic and the mechanical aperture is evident in Figure 5. Similar to isolated pores in porous media, open parts of the fracture in Figure 5c create mechanical aperture, but do not contribute to the permeability of the fracture. Thus the mean (i.e. mechanical) aperture is nonzero in Figure 5c whereas the hydraulic aperture is zero.

The effect of fracture closure on the fluid velocity and the fluid pressure distributions is evident in Figures 6 and 7, respectively. The pressure gradient is quite uniform at the beginning of the loading, when the fracture is wide open (Figure 7a). As the loading proceeds, increasingly greater pressure drop is needed to flow through the constriction at the right-hand side of the fracture. As a result, most of the pressure drop occurs at the

right-hand side in Figure 7b. The fluid velocity field becomes increasingly tortuous as the loading proceeds (compare Figure 6b to Figure 6a).

Figure 8 shows the ratio of hydraulic to mechanical aperture, w_h/w , as a function of the mechanical aperture, w . As w increases, w_h/w asymptotically approaches 1, as expected since the effect of roughness decreases with w (the height of asperities becomes *relatively* small, compared to the steadily increasing fracture aperture).

It seems, from the above exposition that the flow stoppage at displacement 2 mm is controlled by the right-hand constriction in the fracture landscape. What if the flow were in the orthogonal direction? Would the results be different? In order to answer this question, flow simulations were repeated in the y -direction for all displacement steps. It turned out that the flow stopped at the next step, i.e. at 3 mm displacement, in this case. The results were in general quite similar to those obtained with the flow in the x -direction. The results obtained with the flow in the x - and y -directions are juxtaposed in Figure 9. A striking similarity exists between the two curves in Figure 9, despite the fact that the numerical model is relatively small (33×33 nodes in the fracture plane), which might be expected to produce greater anisotropy.

As mentioned above, flow in the x -direction stops at displacement 2 mm, while flow in the y -direction stops at displacement 3 mm. A closer look at Figure 5 reveals why and how this happens. It is evident from Figure 5a that percolating clusters in both x - and y -directions do exist at displacement 1 mm. From Figure 5b, a percolating cluster only in the y -direction survives at displacement 2 mm. From Figure 9c, no percolating cluster can be found in the fracture. This is consistent with the difference in the evolution of w_h in the x - and y -directions in Figure 9.

Figure 9 indicates that, although the anisotropy of the fracture permeability is quite small, it is present at all displacement steps. It is instructive to see how the permeability anisotropy evolves as the fracture closes. This is shown in Figure 10 where the anisotropy coefficient is plotted as a function of the mechanical aperture. The permeability coefficient is here defined as the ratio of the hydraulic aperture obtained with the flow in the x -direction to the hydraulic aperture obtained with the flow in the y -direction. Figure 10 suggests that the permeability anisotropy is indeed quite small, and the fracture becomes more isotropic as it opens. In the limit of an infinitely wide fracture, the anisotropy coefficient would be equal to 1 for *any* fracture since the effect of the (finite) roughness becomes negligible as $w \rightarrow \infty$.

To conclude the elastic case, aperture histograms are presented Figure 11 for increasing displacements. The distribution of the aperture changes shape after the fracture faces come into contact. Contact spots emerge as a peak at the leftmost bin in Figure 11c. Concurrently, the distribution acquires a "fat tail" in Figure 11c.

2.3.2 Ductile rock

The material properties used in the simulation of a "ductile rock" are given in Table 2. The rock is linear elastic perfectly plastic, and represents a ductile rock. As evident from Table 2, the elastic properties of the ductile rock were chosen equal to those of the brittle rock (see Section 3.1 and Table 1). This was done in order to single out the effect of rock plasticity on fracture behaviour. Thus, the two cases (ductile vs brittle) differ only with regard to the plastic behaviour, while the elastic properties are identical. In

reality, a "typical" ductile rock would typically have elastic moduli lower than a "typical" brittle rock.

Similarly to the elastic rock, the two rock blocks were initially placed in such way that the initial mechanical aperture was equal to 2 mm. There were no contact spots between the fracture faces at the beginning of the simulation. The displacement of the top surface of the top block was then increased from 0 to 5 mm. After the maximum displacement value of 5 mm had been reached, the applied displacement was decreased through the same steps from 5 mm to 0. After that, a second loading cycle was performed: the displacement was again increased, retracing the same steps from 0 to 5 mm.

Averaged stress at the top surface of the top block *vs* applied displacement is shown in Figure 12. The curve in Figure 12 is nonlinear and has a significantly different shape than the respective curve for an elastic rock (Figure 2, solid line). Namely, the curve is S-shaped during loading of the ductile rock. The nonlinear part at the beginning of the loading in Figure 12 is caused by the same mechanism as the nonlinearity in the case of the elastic rock, i.e. an increase in the contact area. The nonlinear part at the end of the loading (rightmost part of the S-shaped curve in Figure 12) is caused by plastic yield at contact points. Plastic yield leads to the flattening of the fracture faces by the end of the load increase. As a result, the aperture of the fracture is smaller and more evenly distributed than at the end of loading of the elastic model. The hysteresis caused by plastic deformation at the fracture faces is evident in the evolution of the hydraulic aperture (Figure 13). The evolution of w_h during loading resembles that in the elastic rock (cf. Figure 3). However, whereas the same curve would be traced by an elastic rock during unloading as during loading, plastic deformation leads to a hysteretic loop in Figure 13. The unloading branch is reversible. In addition, the unloading branch is linear, apart from a slight nonlinearity at the rightmost end (at the very beginning of unloading). The latter is caused by an elastic rebound of the fracture faces. After that, the two fracture faces become completely separated, and the increase in the aperture follows the displacement applied at the top side of the top block. Irreversible, plastic deformation of asperities experienced during compression in the first cycle results in the hydraulic aperture being virtually equal to the average (i.e. mechanical) aperture during subsequent unloading and reloading. This is evident in Figure 14 (red curve).

The hysteresis evident in Figures 13 and 14 results in different relationships between w_h and w at the initial loading and during subsequent unloading-reloading. During the initial fracture closing, the relationship between w_h and w is similar to that of an elastic rock. During unloading, the fracture surfaces are quite smooth because of the plastic deformation induced in the preceding loading. In subsequent loading cycles, the asperities do not cause so much flow tortuosity as they did in the original fracture, prior to the first loading cycle. Thus, repeated normal loading/unloading of a ductile rock reduces the permeability anisotropy of a fracture.

In addition to affecting the value of the hydraulic aperture, the repeated loading also affects the anisotropy of the fracture permeability. It is evident from Figure 14 that the fracture was slightly anisotropic during the initial loading, just as its elastic counterpart was. During unloading and subsequent reloading, the fracture opened for flow, and its permeability was virtually identical in the x - and y -directions since the asperities were smoothed out by plastic deformation, and their impact on the flow tortuosity was thereby significantly reduced.

To conclude the ductile case, aperture histograms are presented Figure 15 for successive loading and unloading steps in the first cycle. Note that the initial distribution, prior to the first cycle, is identical to the brittle case and is shown in Figure 11a. After the fracture faces come into contact, the distribution rapidly changes shape acquiring a fat tail in Figure 15b, just as it did in the brittle rock. During unloading, an elastic rebound occurs, and the distribution becomes quite close to normal in Figure 15c. The distribution of the aperture in the fracture that experienced plastic deformation is much narrower than it was in the original fracture (notice the scale of the horizontal axis in Figures 15b and 15c). Subsequent parting of the faces of the already opened fracture shifts the distribution towards higher apertures without altering its shape (Figure 15d).

2.4 Discussion

Hysteresis in the fracture permeability *vs* normal stress exhibited by the ductile rock suggests that caution should be exercised when transferring the results of laboratory measurements of the fracture permeability under stress onto in-situ (reservoir) conditions. The rock could have been subject to a complex loading history in situ. Performing a single loading in the laboratory with an uncomplicated stress path is therefore likely to produce the fracture permeability figures that are not very relevant for an in-situ fracture.

Simulations suggest that there is no direct proportionality between the mechanical and the hydraulic aperture, even if the rock were perfectly elastic. Moreover, there might be a nonzero mechanical aperture below which there is no flow, i.e. below which the hydraulic aperture is zero. This is evident in Figure 8.

The results presented in Figure 8 are inconsistent with the empirical law of (Barton et al. 1985) which suggests that the ratio w_h/w should linearly increase with w :

$$\frac{w_h}{w} = \frac{w}{\text{JRC}^{2.5}} \quad (2)$$

where JRC is the joint roughness coefficient of the fracture surfaces. Earlier, (Chen et al. 2000) pointed out that Barton's formula was inconsistent with their experimental results. In the case of our Figure 8, the inconsistency with Eq. (2) is mainly in the existence of a threshold value of w below which there is no flow in our simulation. This might be the effect of finite fracture dimensions. However, even in a very large fracture, some isolated spots might remain opened after the flow is blocked as the fracture closes, thereby creating some nonzero, "residual" mechanical aperture (similar to isolated pores creating porosity but not contributing to permeability in porous media). Therefore, the existence of a threshold value of w seems plausible albeit contradicting Eq. (2). This is also consistent with the discussion of flow in fractures of correlated *vs* uncorrelated landscapes in (Pyrak-Nolte and Morris 2000). In a fracture having a correlated aperture distribution (or, more precisely, when the correlation radius is the same order of magnitude as the in-plane fracture dimensions), the fluid flow is dominated by few preferential flow paths similar to those appearing in Figure 6b. When these channels are closed during fracture deformation, the flow rate will drop to zero. On the other hand, in the case of uncorrelated landscapes (or, more precisely, in the case of a fracture with large in-plane dimensions compared to the correlation radius), asperities are distributed

evenly across the fracture, and therefore multiple flow paths are available even at large normal displacements.

Different behaviour of the fracture permeability in the first *vs* subsequent loading cycles in the ductile rock suggests that different fracture permeability closure laws might be applicable for mature fractures and fresh (newly created) fractures. The hysteresis in the mechanical behaviour of a fracture and in the fracture permeability under cyclic normal loading is known from experiments. An example is provided in (Gangi 1978) where it was attributed to the breakage of asperities in the first cycle. In our model of the "ductile rock", the asperities irreversibly deform rather than break. It should be noted that irreversible (hysteretic) behaviour of fracture permeability was observed also in experiments on brittle rocks, e.g. (Scholz and Hickman 1983).

Experiments suggest that, in some cases, plasticity at contacts may contribute significantly to fracture-permeability reduction at elevated normal stresses. This is corroborated, for instance, by digital strain imaging of a fracture formed at the interface between cement and rock (Walsh et al. 2012). In the latter experiment, plastic deformation was observed in the amorphous silica regions and regions depleted of Portlandite cement adjacent to the fracture faces. These chemical alterations were induced by exposure to CO₂. As a result, the reduction in the fracture permeability under stress was significantly greater than what could be attributed to the elastic deformation of contacts alone.

In real rock formations, the flattening effect observed in the simulation on the ductile rock and caused by plastic deformation of asperities, could be further enhanced by shear displacement under stress that may further smooth the fracture faces out by shearing the asperities off. The gouge (pieces of broken rock) produced during such slip may further complicate the picture by blocking the flow in the fracture and thereby reducing the fracture permeability (Lorenz 1999; Smart et al. 2001).

The changes of the aperture distribution as the fracture closes (see the histogram evolution from Figure 11a to Figure 11c) is quite similar to the changes observed in experiments by Muralidharan et al., who used CT scans to quantify the development of fracture aperture under normal stress (Muralidharan et al. 2004). In particular, the emergence of the "fat tail" in the distribution evident in our Figure 11c (and Figure 15b) was observed in Muralidharan et al.'s experiments.

The effect of irreversible, plastic normal deformation on the fracture aperture is to compress the statistical distribution of the aperture, so that the apertures fall into a narrower range than they do in a virgin fracture (Figure 15). The statistical distribution of apertures in a fracture that underwent plastic deformation is different than it was before such deformation. The loading of a fractured rock leaves therefore an "imprint", or "memory", about the loading that then stays in the fracture. The roughness of the fracture faces thus carries information about the stress history. This is in a way similar to other stress-memory effects in rocks, such as the Kaiser effect in acoustic emission, a phenomenon well-known in rock mechanics (Becker et al. 2010; Lavrov 2003).

Fracture permeability is often anisotropic. For instance, anisotropy can be created by shear displacement (slip) of the fracture faces (Detwiler and Morris 2014). Our simulations show that normal loading is likely to increase the anisotropy of the fracture

permeability. This confirms the earlier results of Detwiler and Morris obtained with a much simpler fracture deformation model (Detwiler and Morris 2014).

It should be noted that properties of the rock were identical in the entire rock block in this study. In reality, fracture surfaces can be weathered or damaged, making the strength and stiffness of asperities different from the properties of the bulk material. Incorporating such alterations into the finite-element model of fracture deformation should be trivial, but would require information about the distribution of, e.g., cohesion and internal friction angle in the rock, in the direction normal to the fracture face. Such information could be obtained, e.g., by a hardness test or a scratch test that enable estimation of rock properties at different depths from the free surface.

In order to use the proposed computational approach, a validation against experiments is needed. Calibration and validation of the model against experiments for specific rocks is an outstanding task. In order to perform such a calibration properly, a larger fracture model would need to be used.

2.5 Conclusions

A computational framework for evaluating the fracture permeability under normal stress has been developed and tested on two examples: a perfectly elastic ("brittle") rock and an elastic perfectly plastic ("ductile") rock. The two types of rock exhibit significantly different behaviour of fracture permeability under repeated loading. Both mechanical and hydraulic behaviour of the fracture under cyclic normal loading are found to be in qualitative agreement with the results obtained in a number of published experimental studies. The computational approach provides an insight into the actual mechanics of the fracture deformation under stress, and the effect of the latter on the permeability. In particular, a hysteresis in the fracture roughness is obtained with the "ductile rock" suggesting that (at least some) fractured rocks may have "memory" about their loading history imprinted in the fracture landscapes. The anisotropy of fracture permeability is reduced as the fracture opens and is increased as the normal stress increases. During repeated loading/unloading of a fracture in a ductile rock, asperities are smoothed out. Therefore, repeated loading/unloading cycles reduce the flow tortuosity and the anisotropy of the fracture permeability. The effect of repeated loading of a ductile rock is also to compress the statistical distribution of the local fracture apertures.

References

- Aguilera R (1980) Naturally fractured reservoirs. The Petroleum Publishing Company, Tulsa
- Aybar U, Eshkalak MO, Sepehrnoori K, Patzek TW (2014) The effect of natural fracture's closure on long-term gas production from unconventional resources Journal of Natural Gas Science and Engineering 21:1205-1213 doi:<http://dx.doi.org/10.1016/j.jngse.2014.09.030>
- Barton N, Bandis S, Bakhtar K (1985) Strength, deformation and conductivity coupling of rock joints International Journal of Rock Mechanics and Mining Sciences & Geomechanics Abstracts 22:121-140 doi:[http://dx.doi.org/10.1016/0148-9062\(85\)93227-9](http://dx.doi.org/10.1016/0148-9062(85)93227-9)

- Bauget F, Fourar M (2008) Non-Fickian dispersion in a single fracture Journal of Contaminant Hydrology 100:137-148 doi:<http://dx.doi.org/10.1016/j.jconhyd.2008.06.005>
- Becker D, Cailleau B, Dahm T, Shapiro S, Kaiser D (2010) Stress triggering and stress memory observed from acoustic emission records in a salt mine Geophysical Journal International 182:933-948 doi:10.1111/j.1365-246X.2010.04642.x
- Brown SR (1987) Fluid flow through rock joints: the effect of surface roughness J Geophys Res B 92:1337-1347
- Brown SR, Scholz CH (1986) Closure of rock joints Journal of Geophysical Research: Solid Earth 91:4939-4948 doi:10.1029/JB091iB05p04939
- Chen Z, Narayan SP, Yang Z, Rahman SS (2000) An experimental investigation of hydraulic behaviour of fractures and joints in granitic rock International Journal of Rock Mechanics and Mining Sciences 37:1061-1071 doi:[http://dx.doi.org/10.1016/S1365-1609\(00\)00039-3](http://dx.doi.org/10.1016/S1365-1609(00)00039-3)
- Cumbie DH, McKay LD (1999) Influence of diameter on particle transport in a fractured shale saprolite Journal of Contaminant Hydrology 37:139-157 doi:[http://dx.doi.org/10.1016/S0169-7722\(98\)00156-9](http://dx.doi.org/10.1016/S0169-7722(98)00156-9)
- Cuss RJ, Milodowski A, Harrington JF (2011) Fracture transmissivity as a function of normal and shear stress: First results in Opalinus Clay Physics and Chemistry of the Earth, Parts A/B/C 36:1960-1971 doi:<http://dx.doi.org/10.1016/j.pce.2011.07.080>
- Detwiler RL, Morris JP (2014) Transmissivity anisotropy in rough-walled fractures: The combined influence of shear offset and normal deformation. Paper ARMA 14-7539 presented at the 48th US Rock Mechanics / Geomechanics Symposium held in Minneapolis, MN, USA, 1-4 June 2014.
- Fournier A, Fussell D, Carpenter L (1982) Computer rendering of stochastic models Commun ACM 25:371-384 doi:10.1145/358523.358553
- Gangi AF (1978) Variation of whole and fractured porous rock permeability with confining pressure International Journal of Rock Mechanics and Mining Sciences & Geomechanics Abstracts 15:249-257 doi:[http://dx.doi.org/10.1016/0148-9062\(78\)90957-9](http://dx.doi.org/10.1016/0148-9062(78)90957-9)
- Gutierrez M, Øino LE, Nygård R (2000) Stress-dependent permeability of a de-mineralised fracture in shale Marine and Petroleum Geology 17:895-907 doi:[http://dx.doi.org/10.1016/S0264-8172\(00\)00027-1](http://dx.doi.org/10.1016/S0264-8172(00)00027-1)
- Keller AA, Roberts PV, Blunt MJ (1999) Effect of fracture aperture variations on the dispersion of contaminants Water Resources Research 35:55-63 doi:10.1029/1998wr900041
- Koyama T, Li B, Jiang Y, Jing L (2008) Numerical simulations for the effects of normal loading on particle transport in rock fractures during shear International Journal of Rock Mechanics and Mining Sciences 45:1403-1419 doi:<http://dx.doi.org/10.1016/j.ijrmms.2008.01.018>
- Lavrov A (2003) The Kaiser effect in rocks: principles and stress estimation techniques International Journal of Rock Mechanics and Mining Sciences 40:151-171 doi:[http://dx.doi.org/10.1016/S1365-1609\(02\)00138-7](http://dx.doi.org/10.1016/S1365-1609(02)00138-7)

- Lavrov A (2005) Fracture-induced Physical Phenomena and Memory Effects in Rocks: A Review *Strain* 41:135-149 doi:10.1111/j.1475-1305.2005.00233.x
- Lavrov A (2014) Radial Flow of Non-Newtonian Power-Law Fluid in a Rough-Walled Fracture: Effect of Fluid Rheology *Transp Porous Med* 105:559-570 doi:10.1007/s11242-014-0384-6
- Lespinasse M, Sausse J (2000) Quantification of fluid flow: hydro-mechanical behaviour of different natural rough fractures *Journal of Geochemical Exploration* 69–70:483-486 doi:[http://dx.doi.org/10.1016/S0375-6742\(00\)00111-4](http://dx.doi.org/10.1016/S0375-6742(00)00111-4)
- Lorenz JC (1999) Stress-sensitive reservoirs *Journal of Petroleum Technology* 51:61-63
- Malama B, Kulatilake PHSW (2003) Models for normal fracture deformation under compressive loading *International Journal of Rock Mechanics and Mining Sciences* 40:893-901 doi:[http://dx.doi.org/10.1016/S1365-1609\(03\)00071-6](http://dx.doi.org/10.1016/S1365-1609(03)00071-6)
- Młynarczyk M (2010) Description and classification of rock surfaces by means of laser profilometry and mathematical morphology *International Journal of Rock Mechanics and Mining Sciences* 47:138-149 doi:<http://dx.doi.org/10.1016/j.ijrmms.2009.09.004>
- Muralidharan V, Chakravarthy D, Putra E, Schechter DS (2004) Investigating fracture aperture distributions under various stress conditions using X-ray CT scanner. paper 2004-230 presented at the Petroleum Society's 5th Canadian International Petroleum Conference (55th Annual Technical Meeting), Calgary, Alberta, Canada, June 8-10, 2004.
- Nowamooz A, Radilla G, Fourar M, Berkowitz B (2013) Non-Fickian Transport in Transparent Replicas of Rough-Walled Rock Fractures *Transp Porous Med* 98:651-682 doi:10.1007/s11242-013-0165-7
- Pyrak-Nolte LJ, Morris JP (2000) Single fractures under normal stress: The relation between fracture specific stiffness and fluid flow *International Journal of Rock Mechanics and Mining Sciences* 37:245-262 doi:[http://dx.doi.org/10.1016/S1365-1609\(99\)00104-5](http://dx.doi.org/10.1016/S1365-1609(99)00104-5)
- Schmittbuhl J, Steyer A, Jouniaux L, Toussaint R (2008) Fracture morphology and viscous transport *International Journal of Rock Mechanics and Mining Sciences* 45:422-430 doi:<http://dx.doi.org/10.1016/j.ijrmms.2007.07.007>
- Scholz CH, Hickman SH (1983) Hysteresis in the closure of a nominally flat crack *Journal of Geophysical Research: Solid Earth* 88:6501-6504 doi:10.1029/JB088iB08p06501
- Smart BGD, Somerville JM, Edlman K, Jones C (2001) Stress sensitivity of fractured reservoirs *Journal of Petroleum Science and Engineering* 29:29-37 doi:[http://dx.doi.org/10.1016/S0920-4105\(00\)00088-7](http://dx.doi.org/10.1016/S0920-4105(00)00088-7)
- Twiss RJ, Moores EM (2007) *Structural Geology*, 2nd ed. edn. W.H.Freeman,
- Walsh SDC, Du Frane WL, Sholokhova Y, Settgest R, Johnson SM, Carroll SA (2012) Chemo-mechanical permeability evolution in wellbore-cement fractures exposed to carbon-dioxide-rich brines. Paper ARMA 12-426. Paper presented at the the 46th US Rock Mechanics / Geomechanics Symposium held in Chicago, IL, USA, 24-27 June 2012,
- Zimmerman RW, Kumar S, Bodvarsson GS (1991) Lubrication theory analysis of the permeability of rough-walled fractures *International Journal of Rock Mechanics*

and Mining Sciences & Geomechanics Abstracts 28:325-331
doi:[http://dx.doi.org/10.1016/0148-9062\(91\)90597-F](http://dx.doi.org/10.1016/0148-9062(91)90597-F)

Tables

Table 1. Material properties in the simulation of a "brittle" rock.

Property	Value
Young's modulus, GPa	5.0
Poisson's ratio	0.3

Table 2. Material properties in the simulation with linear elastic perfectly plastic rock.

Property	Value
Young's modulus, GPa	5.0
Poisson's ratio	0.3
Cohesion, MPa	5.0
Angle of internal friction, °	30
Angle of dilatancy, °	25

Figures

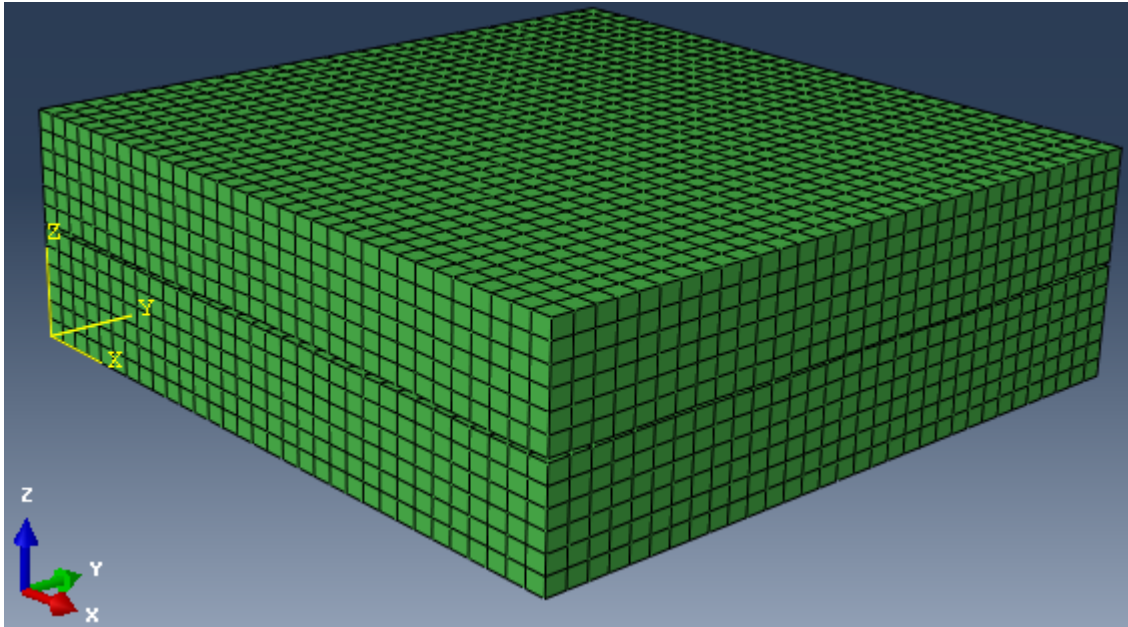


Fig. 1 Two rock blocks with the fracture between them

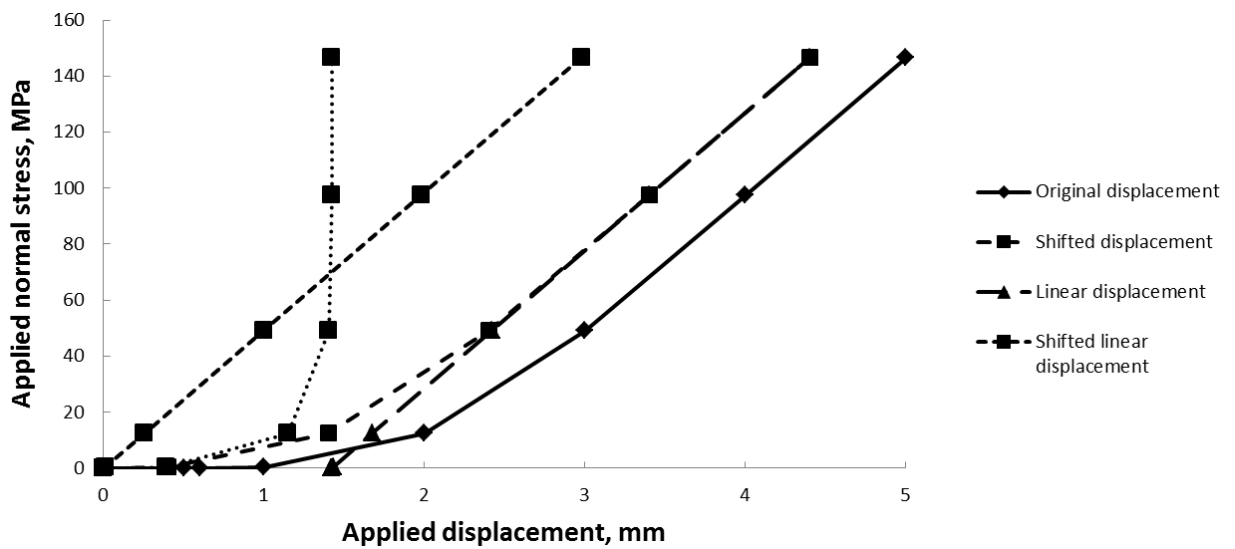


Fig. 2 Stress vs displacement obtained in the simulation of a "brittle" rock

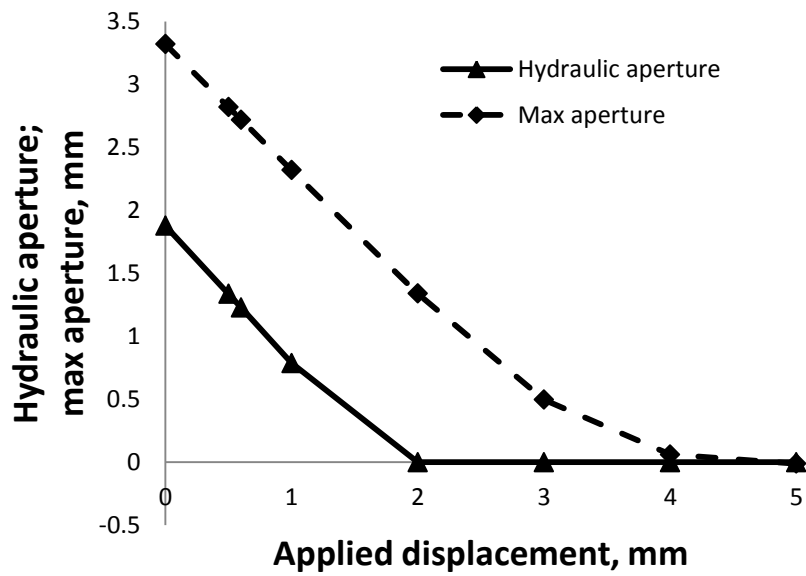


Fig. 3 Hydraulic and maximum apertures vs applied displacement obtained in the simulation of a "brittle" rock. Hydraulic aperture obtained with for flow in *x*-direction

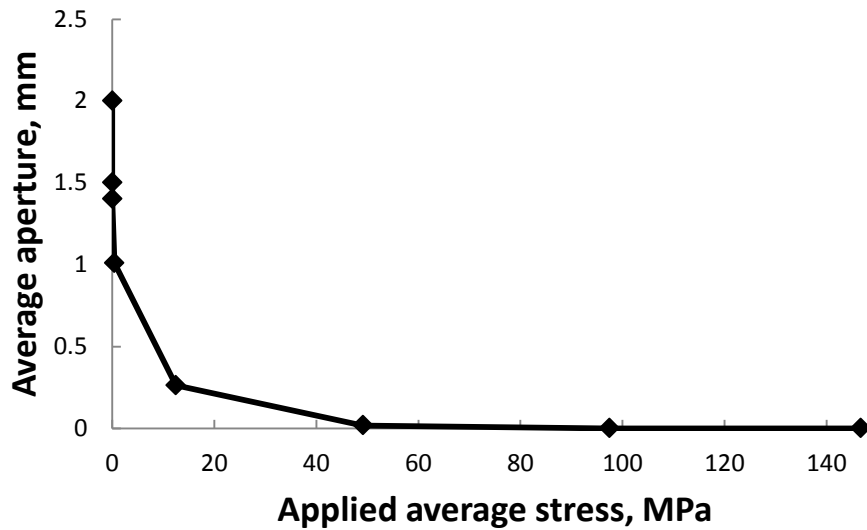
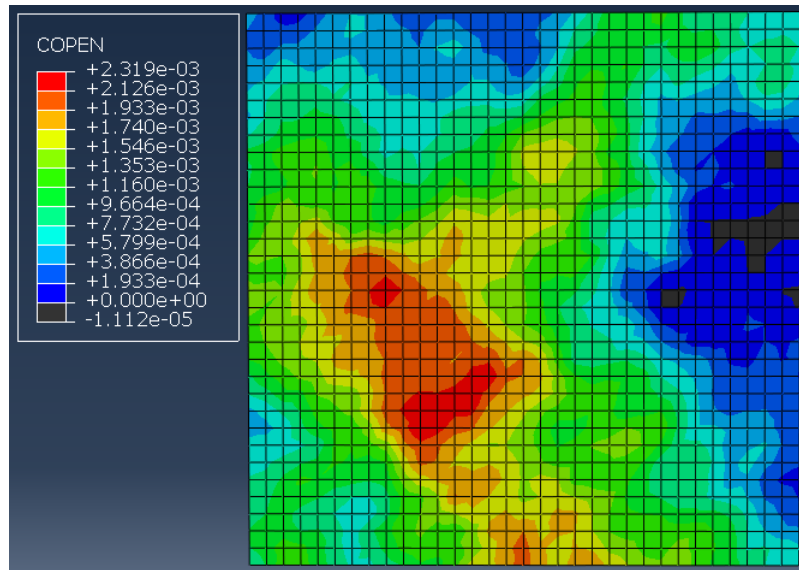
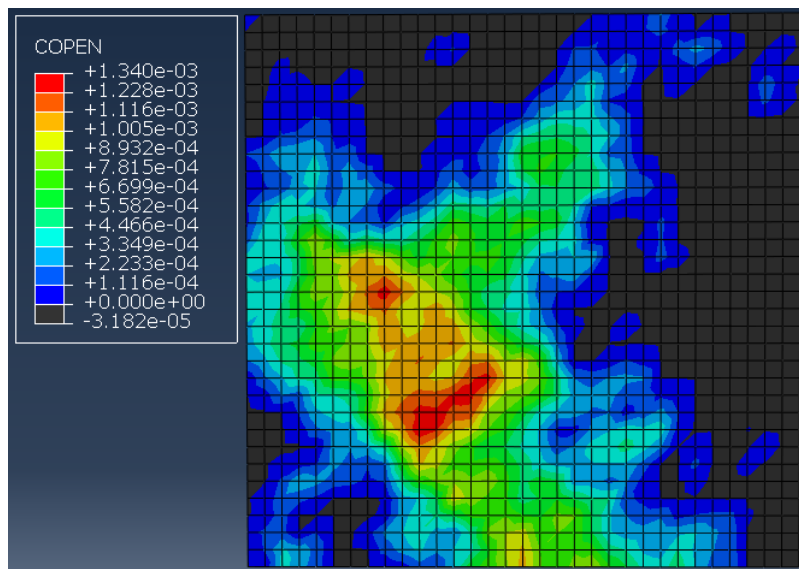


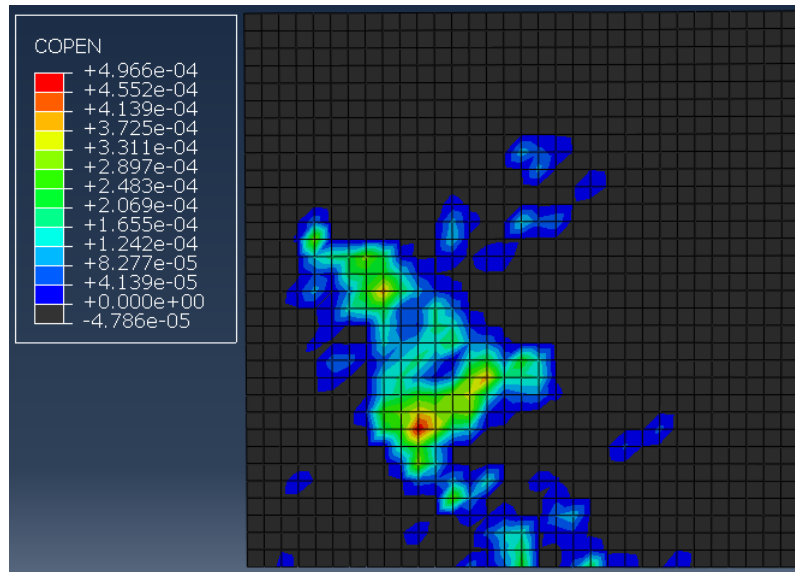
Fig. 4 Average aperture vs applied normal stress obtained in the simulation of a "brittle" rock



a



b



c

Fig. 5 Fracture aperture distributions at successive applied displacements in the simulation of a "brittle" rock (unit of aperture in the legend: m). Dark grey areas: closed fracture (contact between the faces). Axis directions: *x* vertical, *y* horizontal (cf. Figure 1).

- (a) displacement 1.0 mm;
- (b) displacement 2.0 mm;
- (c) displacement 3.0 mm

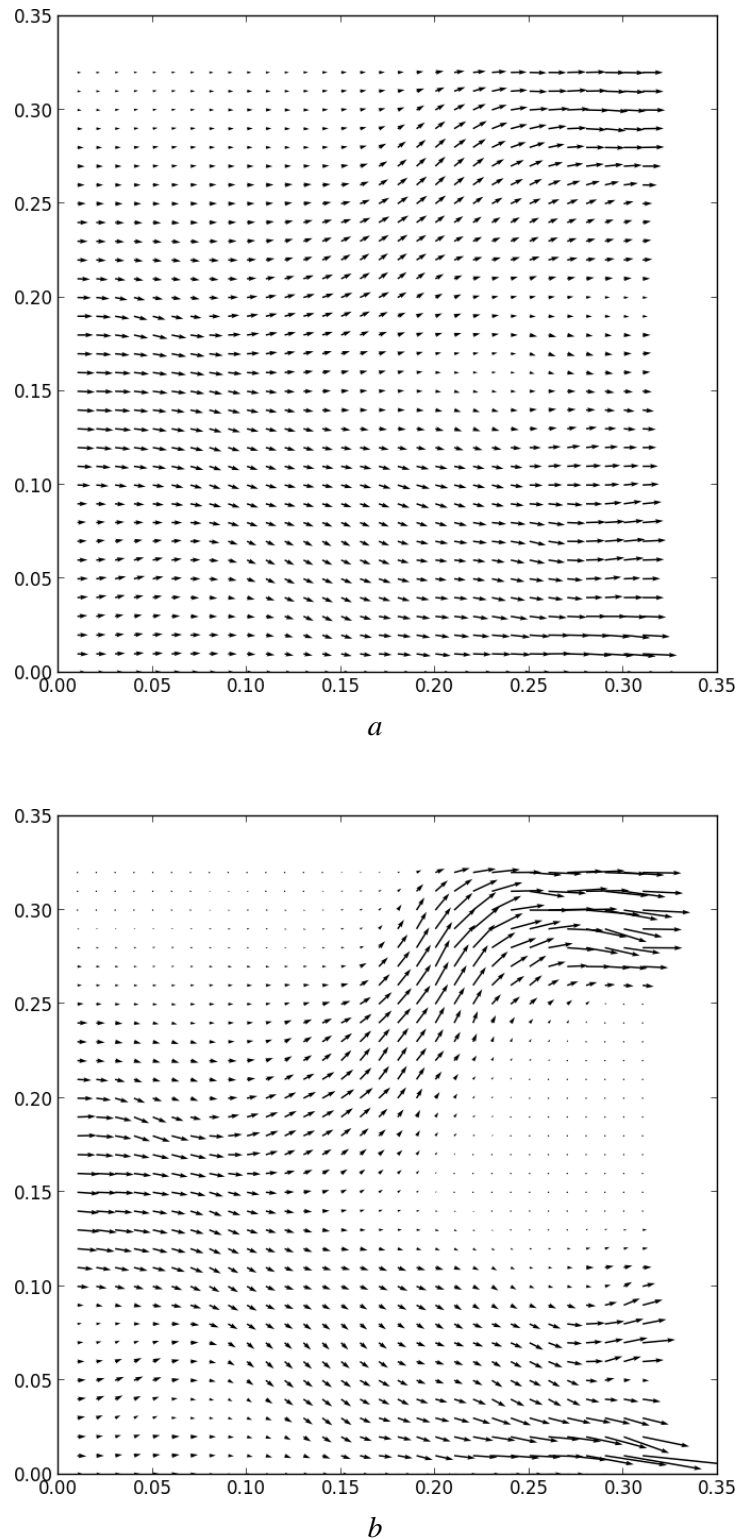


Fig. 6 Fluid velocity distributions at successive applied displacements in the simulation of a "brittle" rock. Units along x - and y -axes are m. Axis directions: x vertical, y horizontal (cf. Figure 1).

- (a) initial state, zero displacement of top surface;
- (b) displacement 1.0 mm

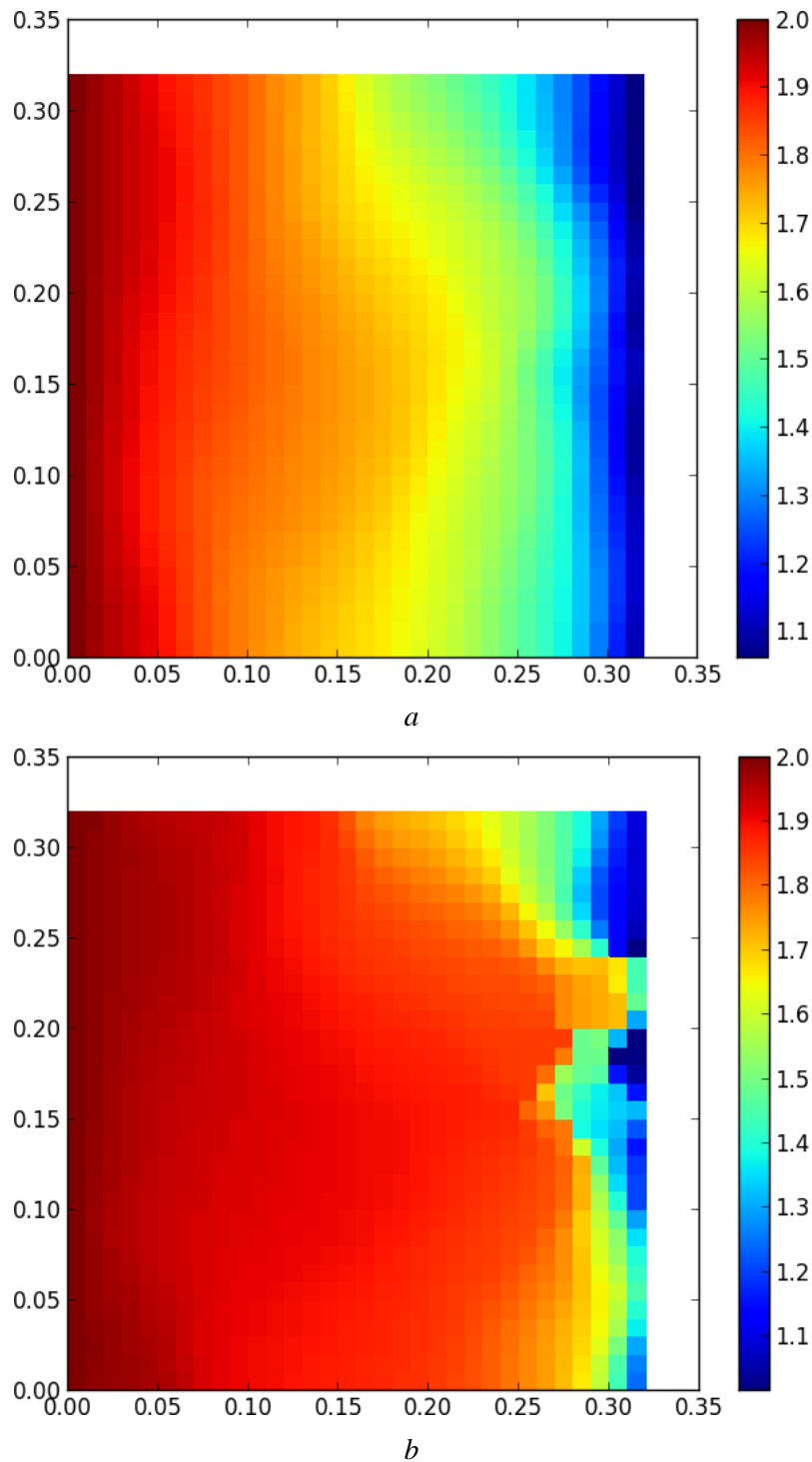


Fig. 7 Fluid pressure distributions at successive applied displacements in the simulation of a "brittle" rock. Units along x - and y -axes are m. Pressure units in the legend are Pa. Pressure applied at the left-hand boundary is 2 Pa. Pressure applied at the right-hand boundary is 1 Pa. Axis directions: x vertical, y horizontal (cf. Figure 1).

- (a) initial state, zero displacement of top surface;
- (b) displacement 1.0 mm

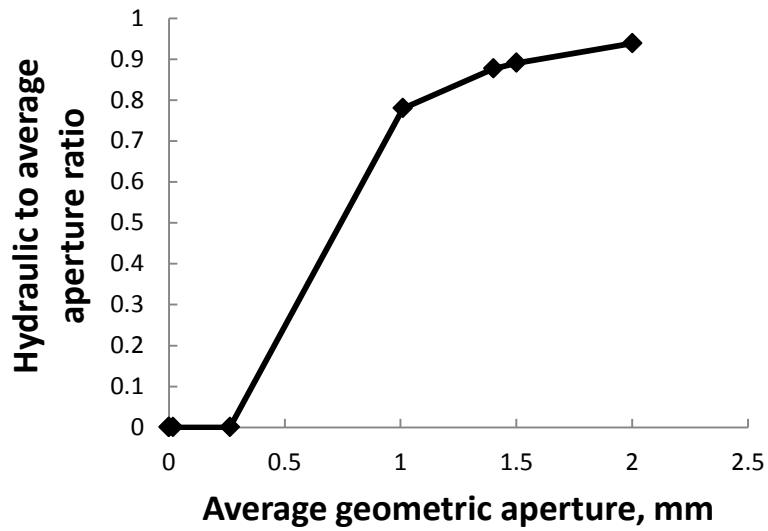


Fig. 8 Hydraulic-to-average aperture ratio vs average aperture in the simulation of a "brittle" rock

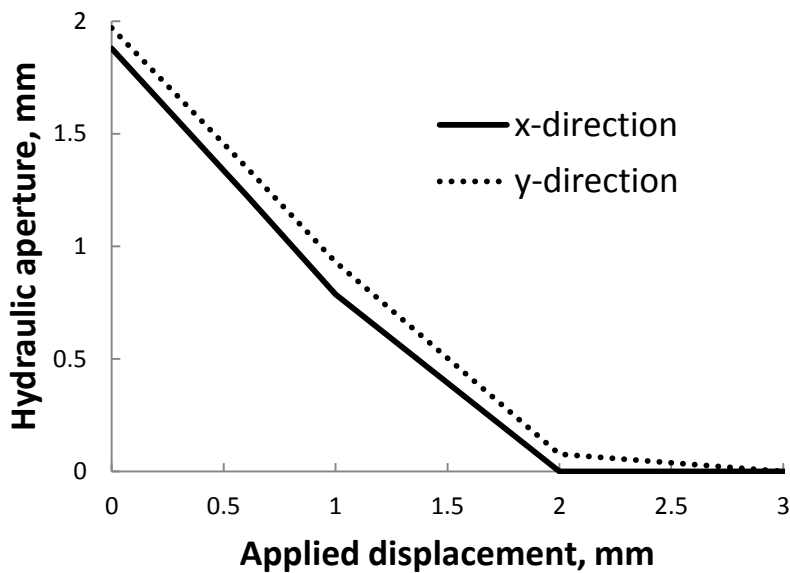


Fig. 9 Hydraulic aperture obtained with flow in *x*- or *y*-direction vs applied displacement in the simulation of a "brittle" rock

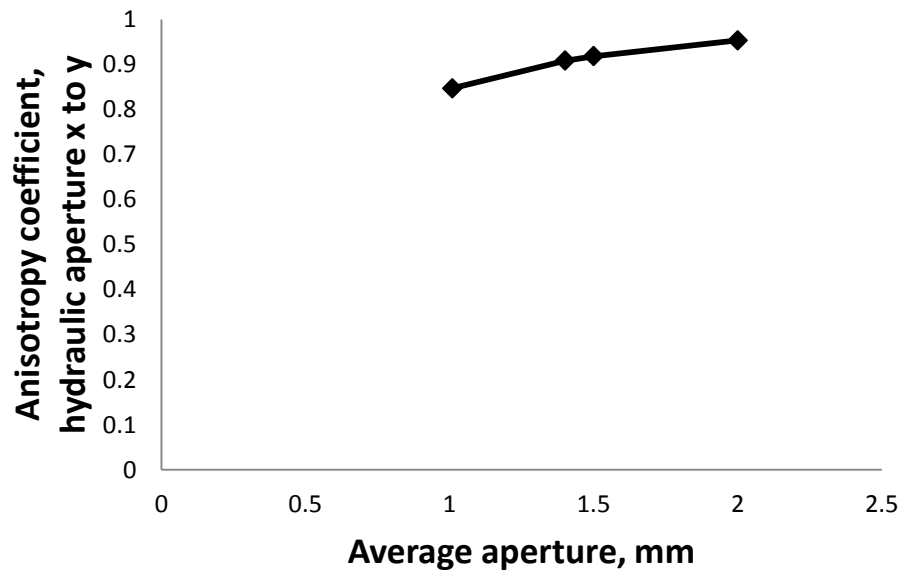
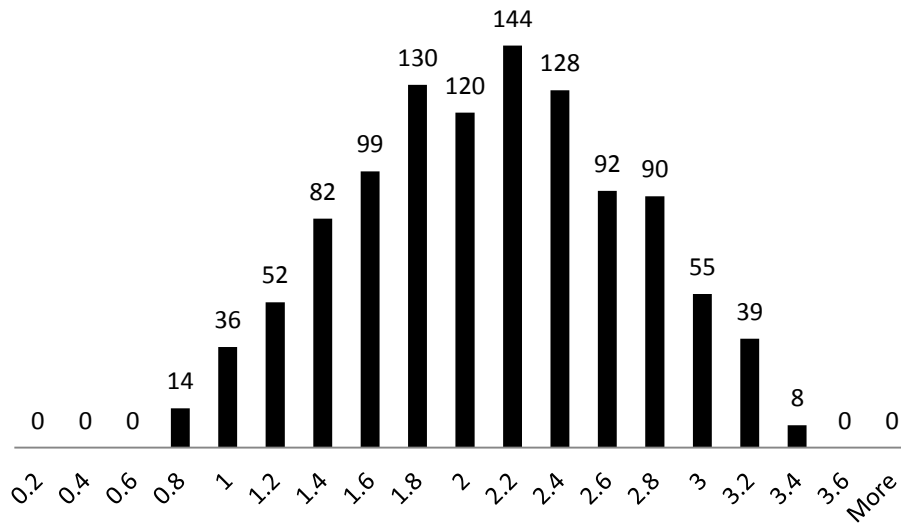
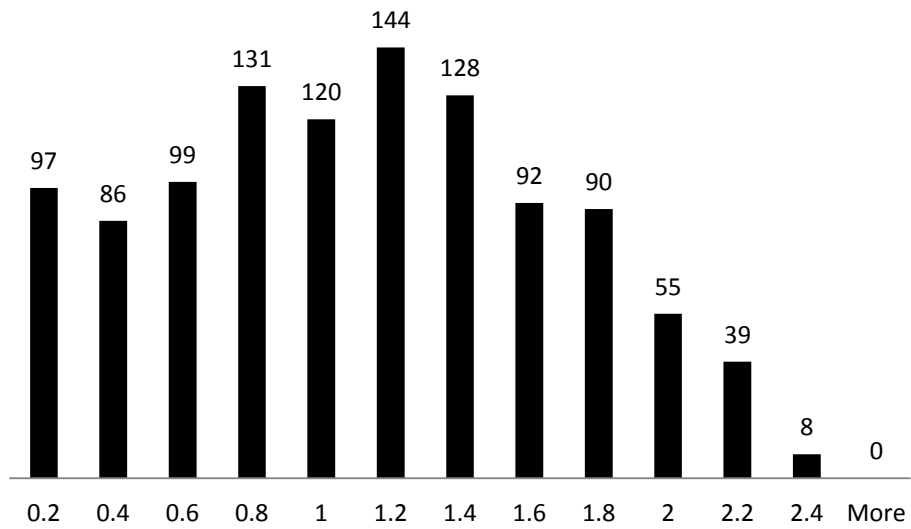


Fig. 10 Anisotropy coefficient vs average aperture in the simulation of a "brittle" rock



a



b

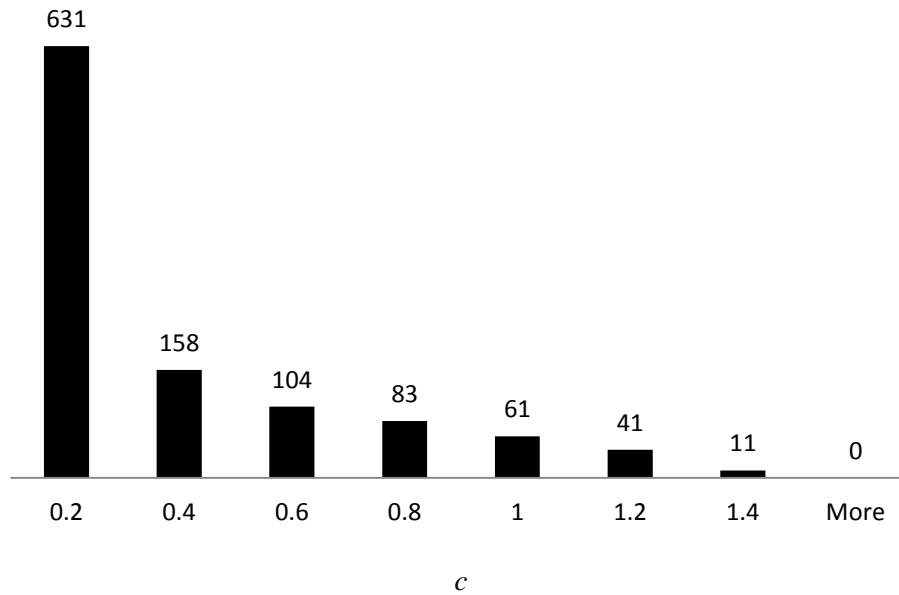


Fig. 11 Histograms of mechanical aperture (mm) at successive applied displacements in the simulation of a "brittle" rock:

- (a) initial state, zero displacement of top surface;
- (b) displacement 1.0 mm;
- (c) displacement 2.0 mm

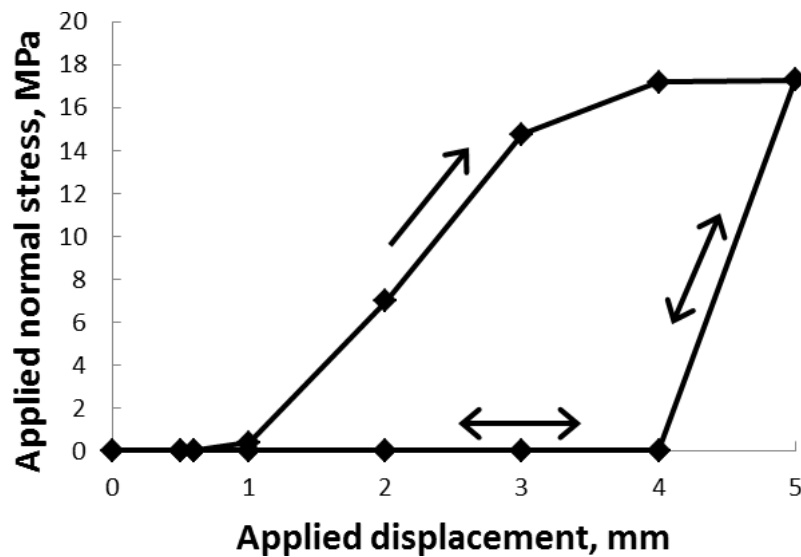


Fig. 12 Stress vs applied displacement in the simulation of a "ductile" rock

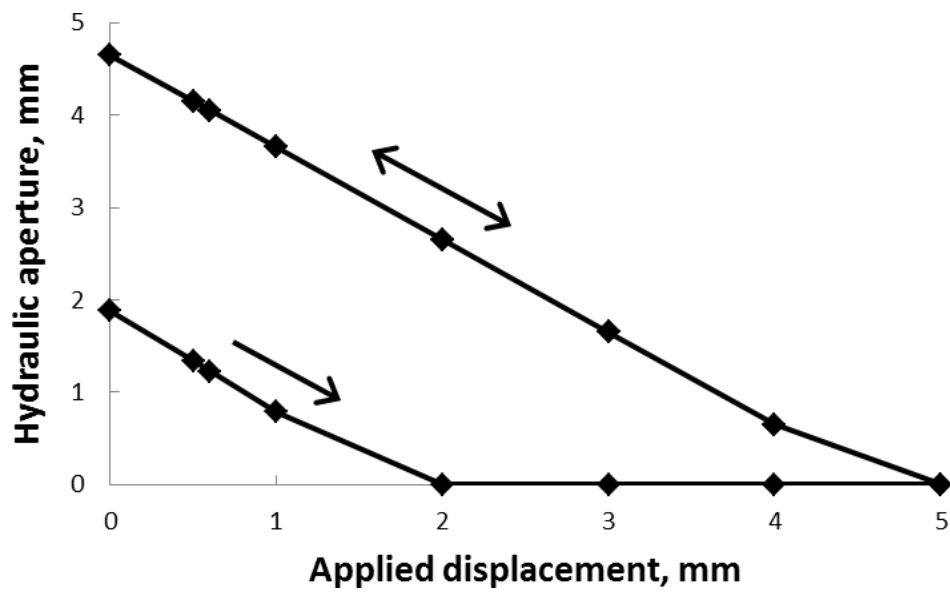


Fig. 13 Hydraulic aperture vs applied displacement in the simulation of a "ductile" rock

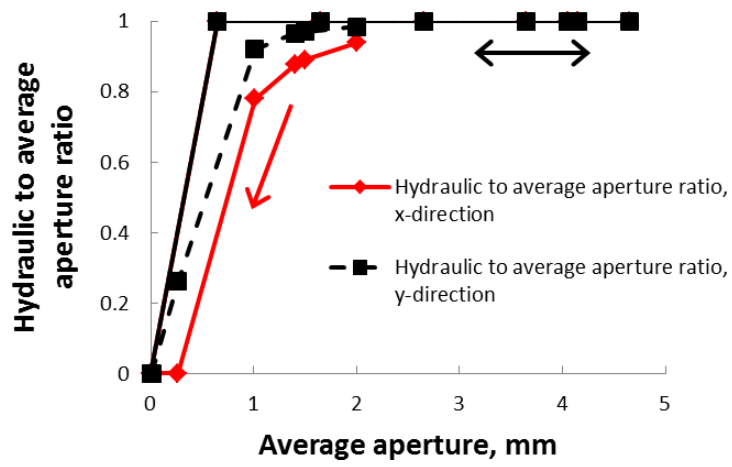
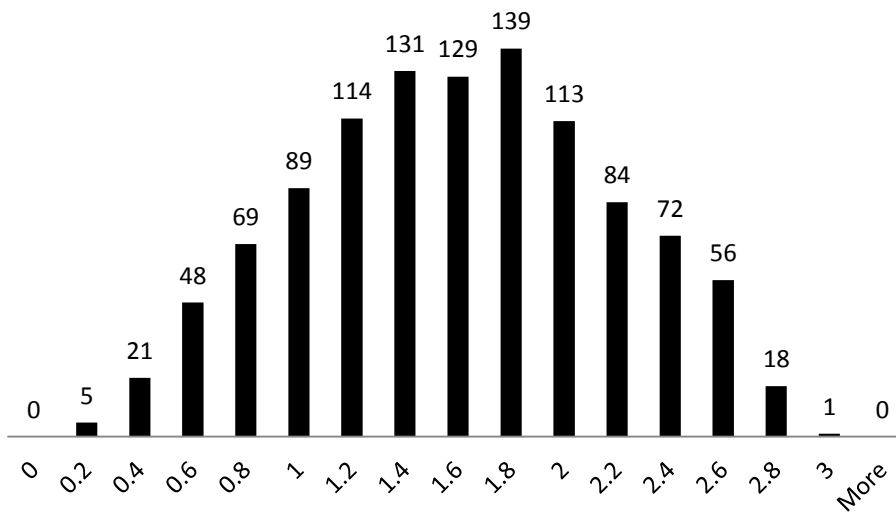
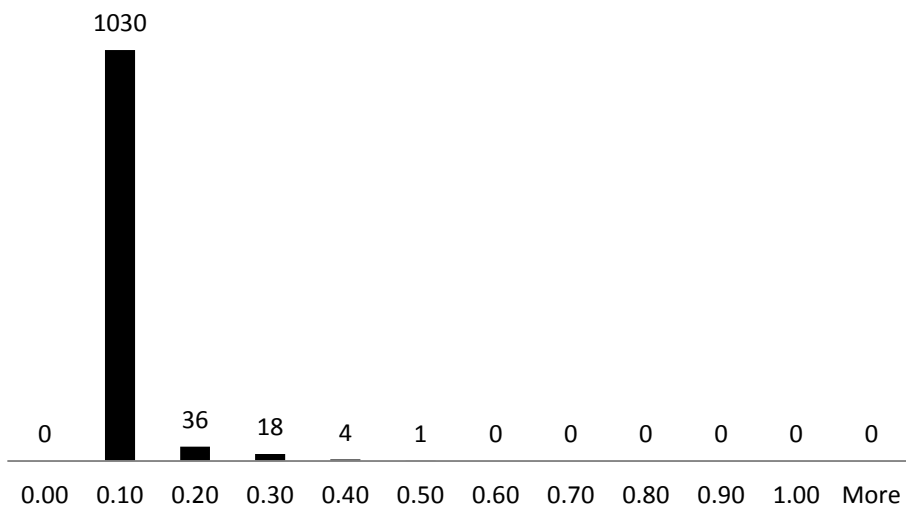


Fig. 14 Hydraulic-to-average-aperture ratio (flow in *x*- or *y*-direction) vs average (i.e. mechanical) aperture in the simulation of a "ductile" rock



a



b

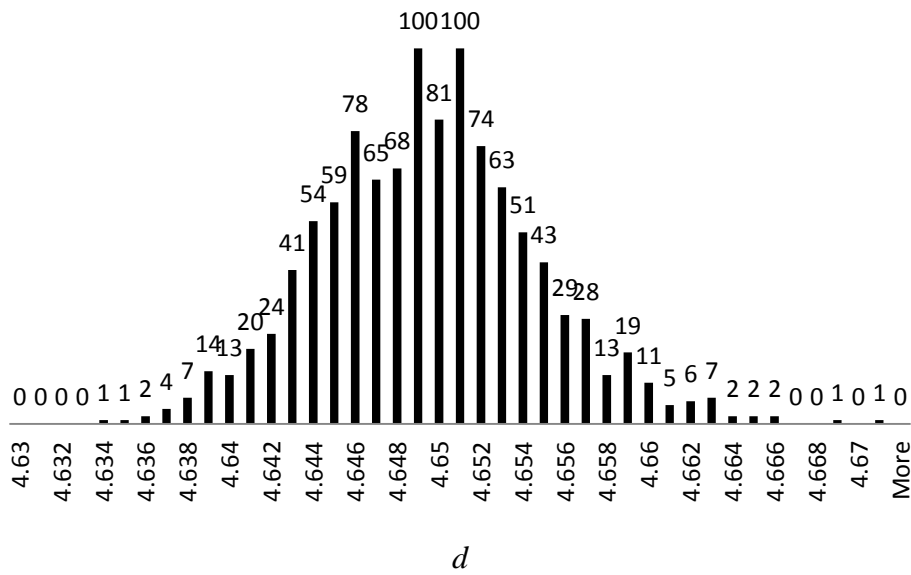
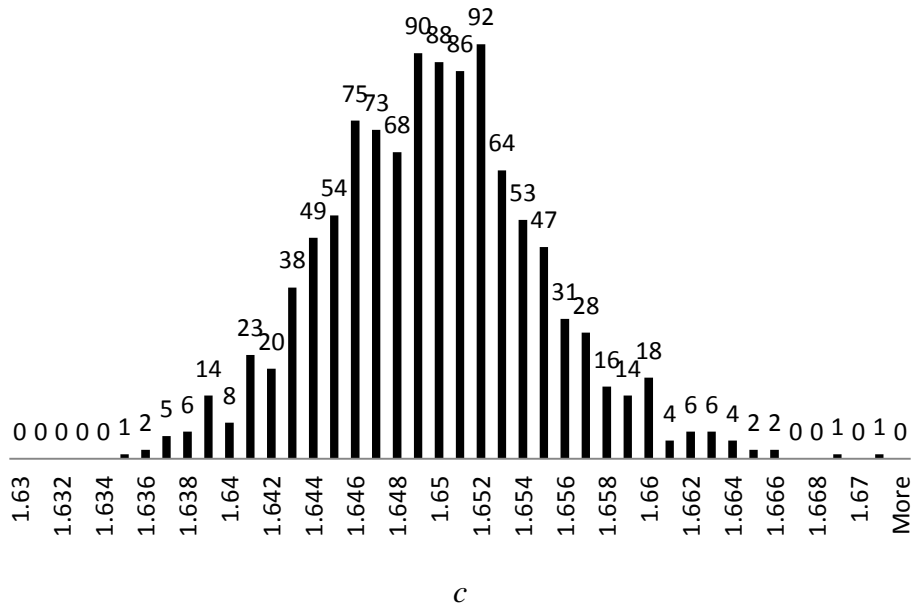


Fig. 15 Histograms of mechanical aperture (mm) at successive applied displacements in the simulation of a "ductile" rock.

- (a) displacement 1.0 mm, loading (first cycle);
- (b) displacement 3.0 mm, loading (first cycle);
- (c) displacement 3.0 mm, unloading (first cycle);
- (d) zero displacement, end of unloading from the first cycle

3 COUPLED NUMERICAL MODELLING OF STRESS-DEPENDENT CO₂ FLOW THROUGH FAULTS IN THE CAP ROCK

3.1 Introduction

This part of report describes coupled numerical simulations of stress-dependent CO₂ flow through faults that connect the main storage reservoir with the overlying aquifers. Geological model of the Becej CO₂ gas field [1] was used as a basis to define various simulation cases.

The geological model of the Becej field comprises:

- main gas storage reservoir;
- three shallow aquifers at different depths (-50, -400 and -1200 m);
- four vertical fault zones that connect the main gas reservoir with the shallow aquifers.

Using the coupling of two simulators Eclipse and Visage, we investigated the effect of stress and the associated permeability change on flow rates through faults.

3.2 Simulation cases

For this study a set of simulation cases was defined.

Base case

In the base case, initial pressure in the main reservoir was 151 bar and there was no additional CO₂ injection. Flow simulations were performed by Eclipse without coupling to geomechanics. The permeability update option for the flow through faults was not used here. The amount of CO₂ which migrated through faults to the shallow compartments was calculated without taking into account induced stress changes and the associated permeability changes of faults.

Case 1

In this case two-way coupled hydrodynamic-geomechanical simulations were used to calculate leakage rates assuming the same initial pressure as in the base case and no additional CO₂ injection. Permeability update functions were implemented and used for fault zones. This approach allows a stress-dependent estimate of the amount of CO₂ leakage through faults.

Case 2

Eclipse simulations without coupling to geomechanics were used to assess the case of additional CO₂ injection in the main reservoir. Three wells near the fault zones inject the CO₂ with bottom hole pressure of 250 bars (gas rate unlimited). This causes rapid increase of the reservoir pressure and also enhances the amount of gas leakage through faults.

Cases 3 and 4

These cases use the two-way coupled approach and assume that CO₂ is injected in the main reservoir. The difference between cases 3 and 4 is in the value of a fitting

parameter C used to update permeability function. In case 3, C has a value representative of Kimmeridge shales – 0.27 [2]; in case 4, a value representative of sandstones – 0.4.

3.3 Model setup

3.3.1 Model geometry and flow properties

Previously constructed geological model of the Becej field [1] was used to develop a semi-synthetic model for coupled stress-flow simulations. Because of specific features of Visage simulator, and to reduce calculation times, reservoir simulation grid was simplified. A regular vertical grid was used with cells of 100 m x 100 m (Figure 1). Porosity and permeability were assumed constant for all reservoir layers (Table 1).

Table 1. Porosity and permeability of reservoirs and fault zones.

	Porosity, %	Horizontal permeability, mD	Vertical permeability, mD
Main gas reservoir and shallow aquifers	30	1000	300
Faulted zones	1	1000	0.1

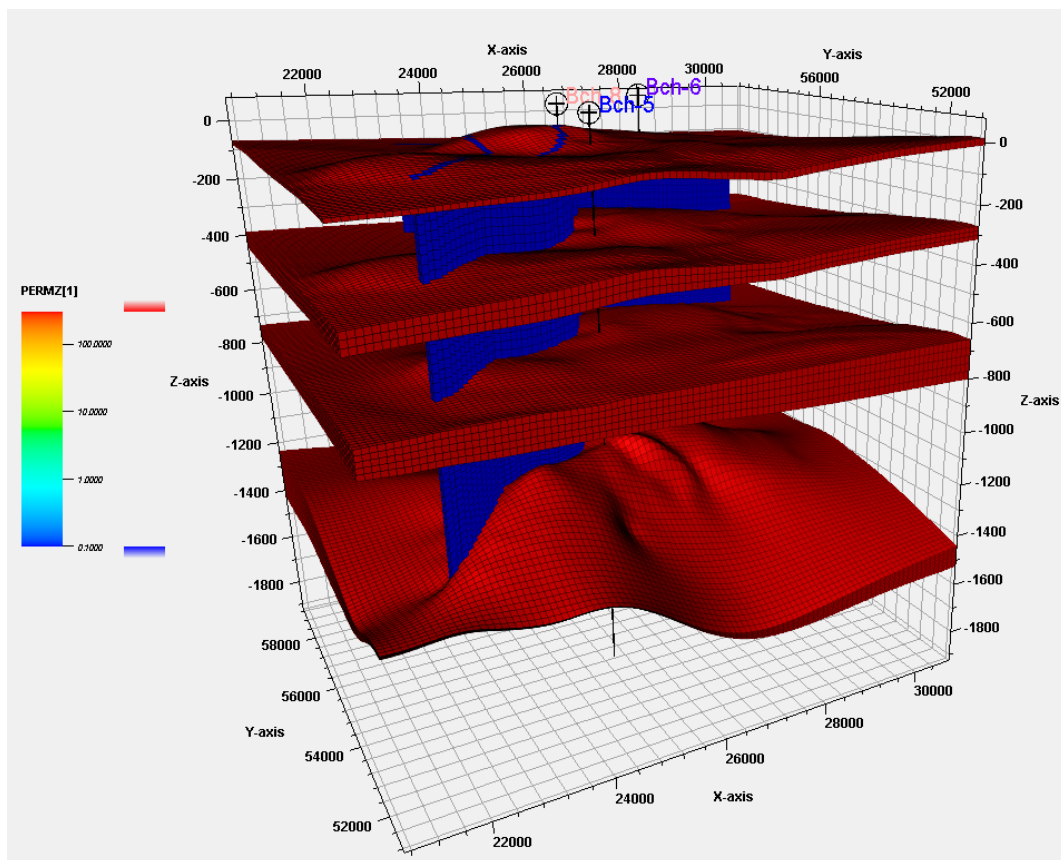


Figure 1: 3D view of the vertical permeability cube.

The fault zones were constructed around the fault surfaces. An additional fault was added near well Bc-6 to have faults in the model, which are oriented parallel and perpendicular to the assumed directions of the principal horizontal *in-situ* stresses. Fault locations are shown in Figure 2.

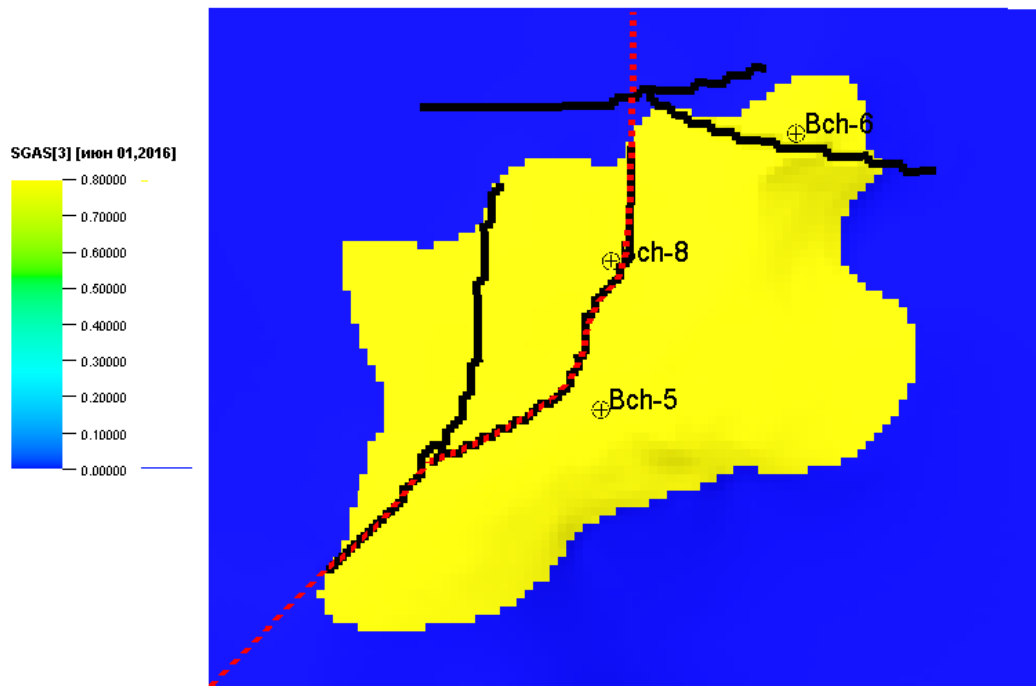


Figure 2: Top view of the main reservoir with faults.

3.3.2 Geomechanical grid

To reduce edge effects in geomechanical simulations, the geological grid was extended by adding the overburden, sideburden and underburden compartments (Figure 3). Size of the resulting geomechanical grid was 70.8 km x 57.5 km x 25 km (Figure 4).

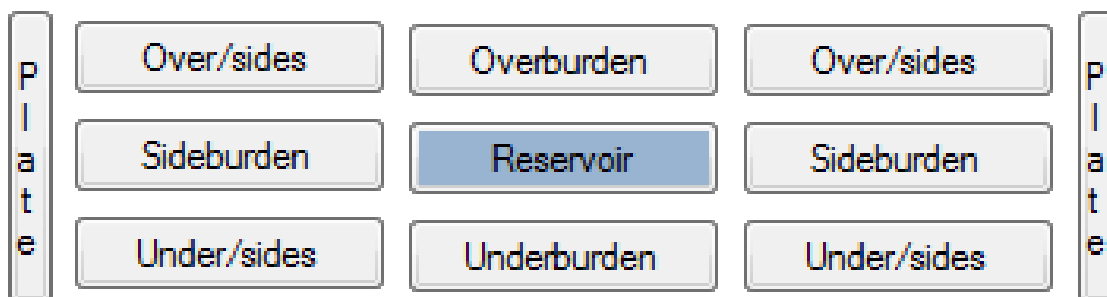


Figure 3: Schematic representation of the geomechanical grid.

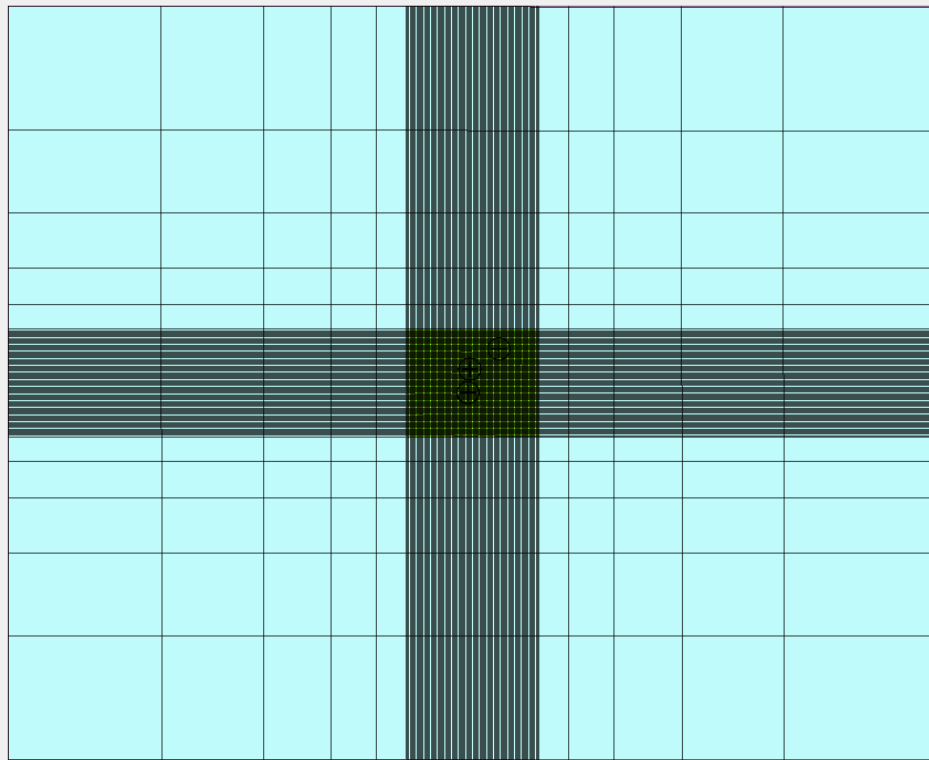


Figure 4: Geomechanical grid.

3.3.3 Geomechanical properties

After building, the geomechanical grid was populated by geomechanical properties. For this purpose the Petrel Reservoir Geomechanics material library was used. For all geological compartments “Sandstones” material was used. Properties of “Steel” were selected for the stiff plates. Elastic properties of materials are listed in Table 2. Yield criteria and material properties are given in Table 3.

Table 2. Elastic properties of model materials.

	Young’s Modulus, GPa	Poisson’s Ratio	Bulk Density, g/cm ³
Sandstones	15.8	0.13	2.45
Steel	200	0.27	7.8

Table 3. Yield criteria and plastic properties of model materials.

Property	Value
Unconfined Compressive Strength, bar	670
Friction Angle, deg	40
Dilation Angle, deg	17.45
Tensile Stress Cut-off, bar	75
Hardening/Softening Coefficient	0

Fault zones were defined as a discontinuity type of material with properties listed in Table 4.

Table 4. Discontinuity properties of fault zones.

Property	Value
Fault normal stiffness, bar/m	20000
Fault shear stiffness, bar/m	10000
Cohesion, bar	0.01
Friction Angle, deg	20
Dilation Angle, deg	10
Tensile Strength, bar	0.01
Initial Opening	0

Young’s modulus (E), Poisson’s ratio (μ) and Unconfined Compressive Strength (q_u) were assumed to be depth-dependent. The values of these parameters were calculated using the following empirical relationships:

$$\begin{aligned}
 E &= 9.16 * \exp(0.004 * D) + 1, \\
 \mu &= -5.75 * 10^{-5} * D + 0.2, \\
 q_u &= (2.28 + 4.1089 * E) * 10,
 \end{aligned}
 \tag{1}$$

where D is the absolute depth. For a depth of 1200 m, the updated value of Young’s modulus amounts to 15.8 GPa and Poisson’s ratio is equal to 0.13.

3.3.4 Permeability update

In two-way coupled simulations, the permeability of fault zones is dependent on shear strain and normal strain. Permeability multipliers used to update normal permeability and shear permeability dependent on shear strain are listed in Table 5 and shown in Figure 5.

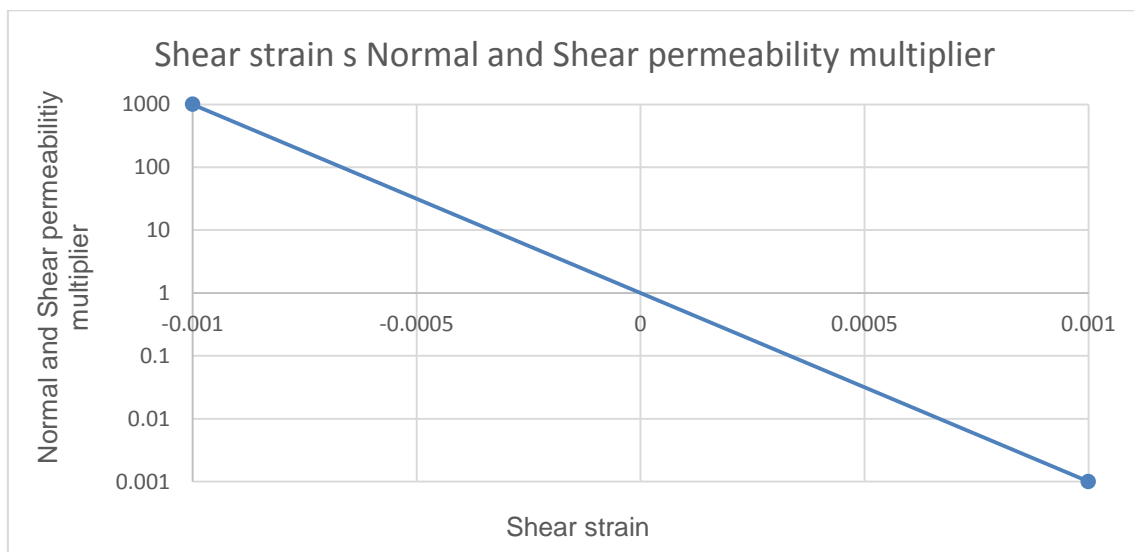


Figure 5: Normal and Shear permeability multiplier vs Shear strain.

Table 5. Shear strain and corresponding Normal and Shear permeability multipliers.

Shear strain	Normal and Shear permeability multiplier
-0.001	1000
0	0
0.001	0.001

Permeability multipliers used to update the shear permeability dependent on normal strain were calculated using the equation given in [2]:

$$k = k_0 \exp(-C'\sigma'_n), \quad (2)$$

where k is the fracture permeability, k_0 is the permeability of a fracture at zero effective normal stress, C' is a fitting parameter and σ'_n is the effective normal stress. Assuming a fault stiffness of 20000 bar/m, the values of permeability multipliers obtained for the two different values of C' are given in Table 6 and Table 7, and shown in Figure 6.

Table 6. Normal strain and corresponding Shear permeability multiplier for $C'= 0.27$, representative of Kimmeridge shale.

Normal strain	Shear permeability multiplier
-0.001	1.71600
0	1
0.0025	0.25924
0.005	0.06720
0.0075	0.01742

Table 7. Normal strain and corresponding Shear permeability multiplier for $C'= 0.4$, representative of sandstone.

Normal strain	Shear permeability multiplier
-0.001	2.2255
0	1
0.0025	0.13533
0.005	0.01831
0.0075	0.00247

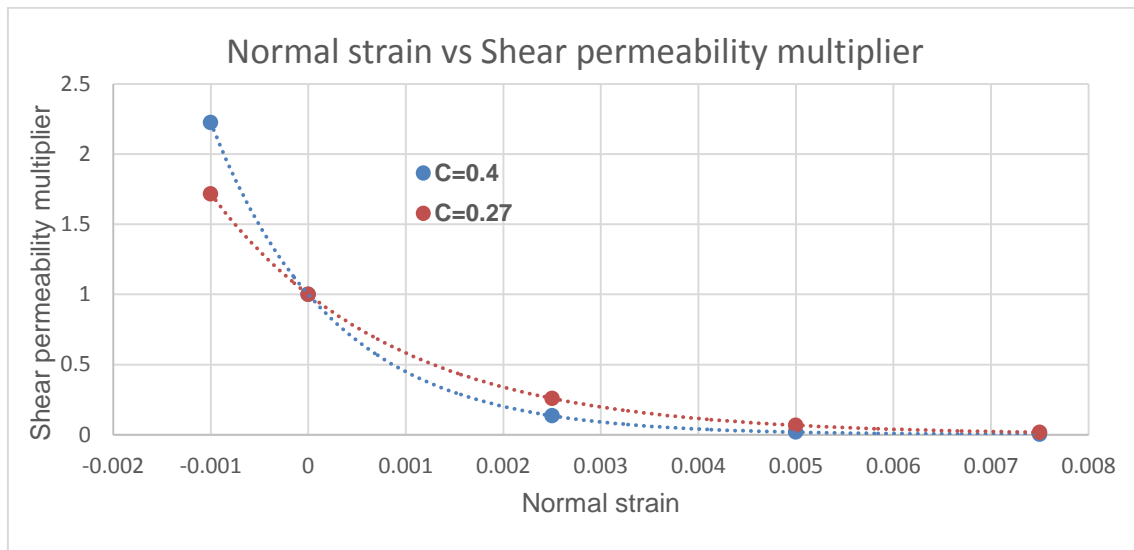


Figure 6: Shear permeability multiplier vs. Normal strain for C' =0.27(red) and C'=0.4(blue).

3.3.5 Geomechanical model initialization

The geomechanical model was initialized by applying the stress conditions determined by the parameters given in Table 8.

Table 8. In-situ stress parameters.

Parameters	Values
Sh gradient, bar/m	0.135
Sh offset, bar	0
SH/Sh	1.15
Sh azimuth, deg	110

3.3.6 Flow model initialization

Reservoir simulation model was initialized as compositional with two components – water and pure CO₂. CO₂-water solubility option was not used.

Shallow aquifers were initialized as separate equilibrium regions with the same pressure and 100% water saturation.

The initial pressure in the main reservoir, at the gas water contact (-1225 m), was 151 bar.

Relative permeabilities were defined by Corey-Brooks correlation for shaly-sand collectors.

The initial gas in place was $89.2 \times 10^9 \text{ m}^3$.

3.4 Simulation results

3.4.1 Cases without gas injection

First we compare results of the cases without CO₂ injection, calculated with uncoupled simulations (base case) and two-way coupled simulations (case 1). The effects of stress-dependent permeability of fault zones on flow rates are plotted in Figure 7.

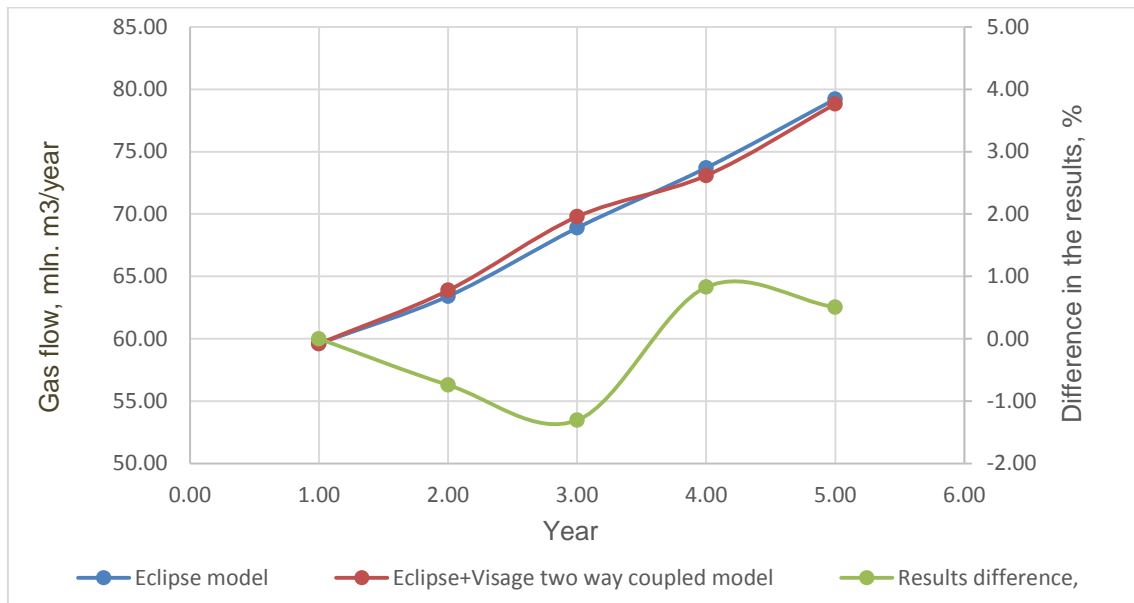


Figure 7: CO₂ flow rates through the central fault from uncoupled (base case) and two-way coupled (case 1) simulations.

Simulation results indicate that the differences in CO₂ flow rates through fault zones in uncoupled and coupled simulations are very small, max 1%. This can be explained by small changes in permeability associated with stress change. During 5 calculation steps, the vertical permeability of some cells decreased from 0.1 mD to 0.083 mD, whereas in other cells the permeability increased to 0.116 (Figure 8). Relatively small increase in fault zone permeability of 16 % had a very small effect on flow rates through fault zones in the model.

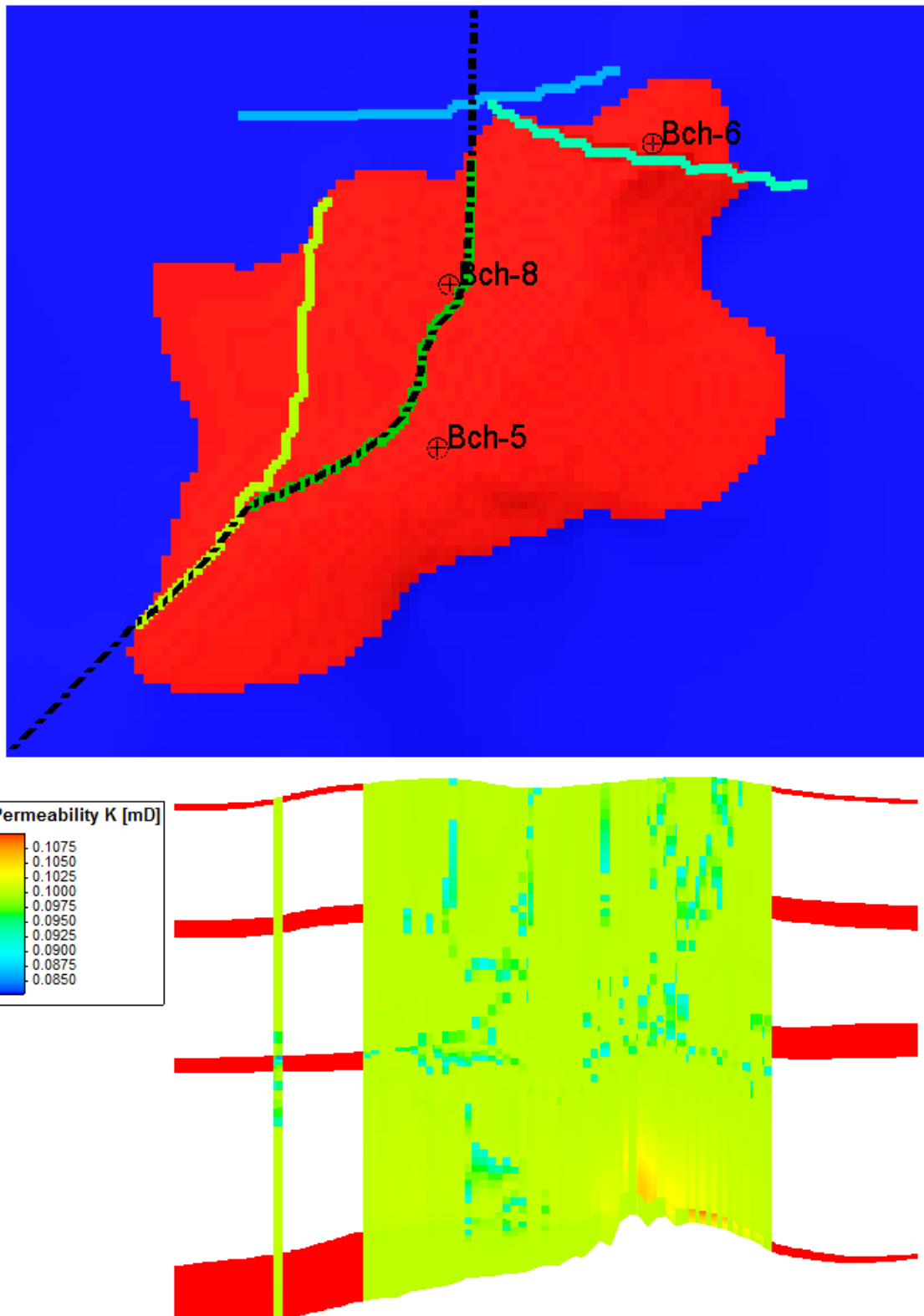


Figure 8: Top view of the main reservoir (top) and vertical cross-section (bottom) showing the vertical permeability cube along the central fault line (indicated by black line in top figure).

3.4.2 Cases with gas injection

In the cases with CO₂ injection (cases 2-4), gas is injected through three wells with constant tubing-hole pressure of 250 bar. The average field pressure increased from the initial 151 bar to 250 bar (Figure 9) and the volume of free gas in the reservoir increased to 151.9*10⁹ m³.

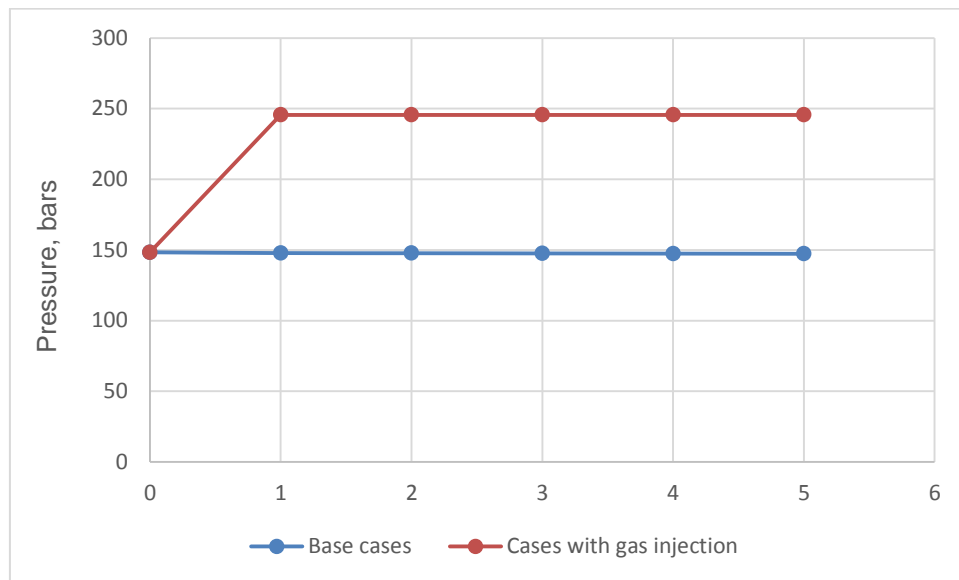


Figure 9: Average field pressure in the main reservoir in the cases without CO₂ injection (blue line) and the cases with CO₂ injection (red line).

Results of the cases with CO₂ injection are compared in Figure 10. Case 2 was calculated with uncoupled simulations, while cases 3 and 4 with coupled simulations.

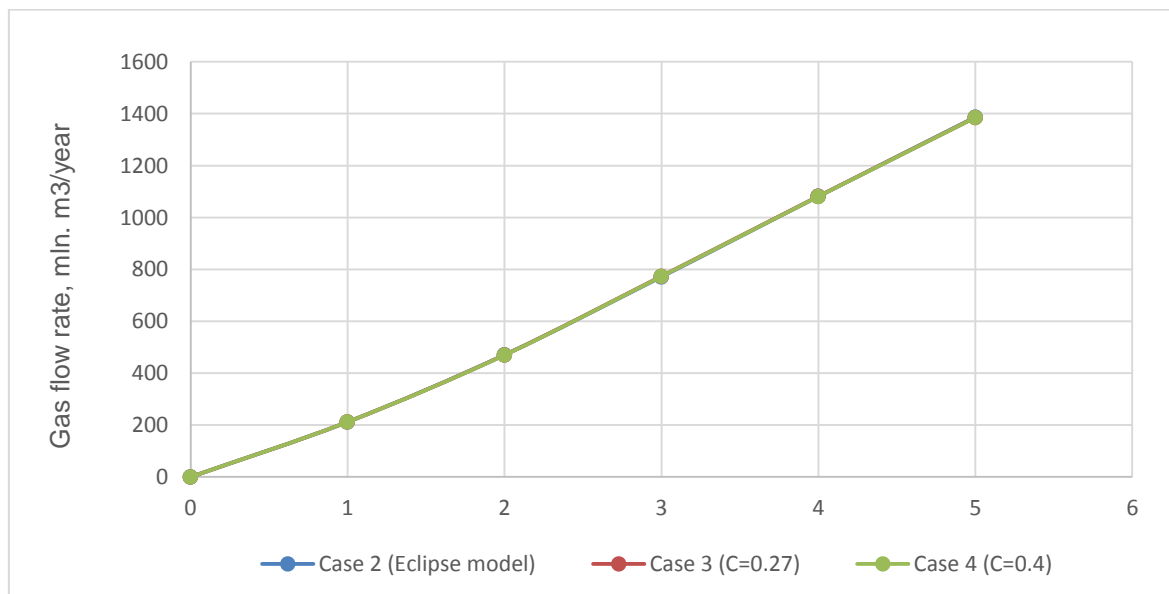


Figure 10: CO₂ flow rates through the central fault from uncoupled simulations(case 2) and coupled simulations(cases 3 and 4). Scenarios 2-4 assume additional CO₂ injection in the main reservoir.

Figures 10 and 11 indicate that the differences between the three cases are very small. This can be explained by very small stress-dependent permeability changes of fault zone (Figure 12). In cases 3 and 4, vertical permeability even decreased from 0.1 mD to 0.08 mD.

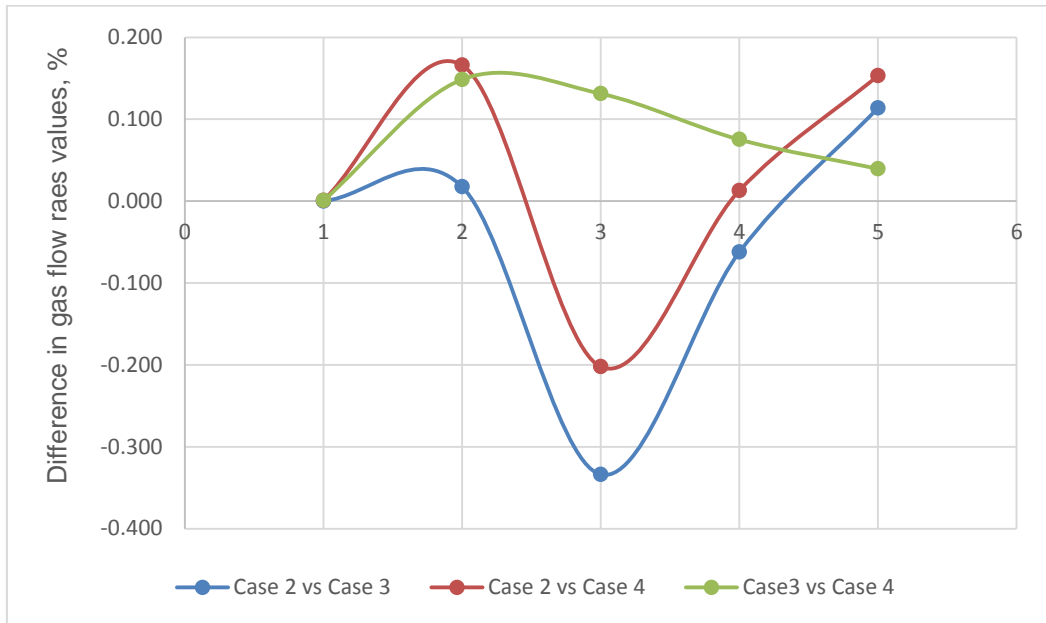


Figure 11: Differences in CO₂ flow rates between different scenarios that assume additional CO₂ injection in the main reservoir.

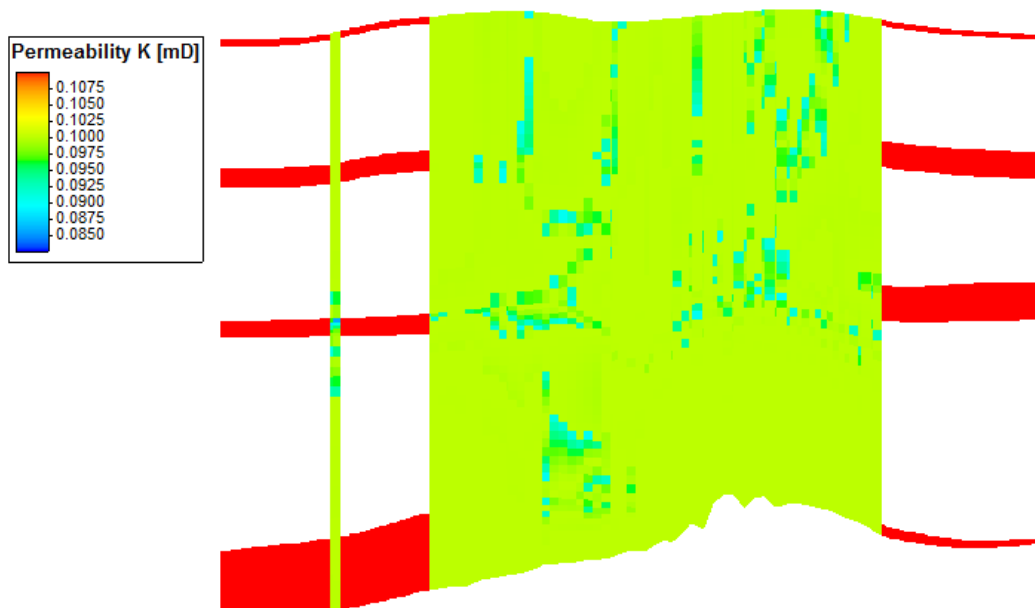


Figure 12: Vertical cross-section showing the vertical permeability cube along the central fault line for case 4.

3.5 Conclusions

Coupled flow-stress simulations were conducted on a semi-synthetic model of the Becej natural CO₂ field to investigate the effect of stress on CO₂ flow rates through a hypothetical fault in the overburden. The workflow for coupled simulations was successfully developed in the Eclipse and Visage simulators. For the simulated cases and the selected ranges of input parameters, the pore pressure changes and the associated stress changes induced very small changes in the fault zone permeability leading to minor changes of flow/leakage rates. The simulation time of 5 years was relatively short, due to long computational times, and should be extended in future simulations.

For future work, we propose to develop a coupled model of stress-dependent CO₂ flow through a single fracture. Multiple fractures could also be introduced to simulate more realistically CO₂ leakage through a fractured fault zone.

References

1. Karas D., Kultysheva K., Demić I., Antropov A., Blagoević M., Pluymaekers M., Orlić B. Pertel model of the Bečej field. Deliverable D12.2 of the MiReCOL project: Mitigation and remediation of leakage from geological storage. 2015.
2. Gutierrez M, Øino LE, Nygård R. Stress-dependent permeability of a de-mineralised fracture in shale. *Marine and Petroleum Geology*. 2000; 17(8):895-907.